Development of a High Energy Resolution Gas Ionization Detector for a Recoil Spectrometer

Jaakko Julin

MSc thesis
Pro gradu -tutkielma
University of Jyväskylä
Department of Physics
June 28, 2011
Supervisor: Timo Sajavaara

Abstract

In this thesis the development of a high energy resolution particle detector and factors affecting the design of such a detector are explained. The particle detector detects particles and measures the kinetic energy of the particle by means of collecting the electrons liberated via ionization in the gaseous medium with an electric field.

The goal of the detector development was to achieve better energy resolution than a planar implanted silicon detector has for heavy ions. The gas ionization detector forms a part of a time-of-flight energy telescope which is used as a recoil spectrometer for Elastic Recoil Detection (ERD). The improved energy resolution improves mass resolution of the telescope and allows heavier recoils to be separated.

Silicon detectors additionally suffer from energy resolution degradation when they are bombarded by heavy ions. A gas ionization detector is radiation hard and the gas can always be changed.

The detector developed at the JYFL accelerator laboratory uses a thin self-supporting silicon nitride entrance window to separate the isobutane used as the working gas from the vacuum of the rest of the telescope. The window thickness ($\leq 100\,\mathrm{nm}$) is crucial to the energy resolution for heavy recoils. Additionally the goal was to have some position sensitivity to enable kinematic correction.

The ionization chamber was successfully designed and built and it achieved superior mass resolution for all elements heavier than helium in comparison with the current system, where a $450\,\mathrm{mm}^2$ Canberra PIPS silicon detector is used as the energy detector.

Tiivistelmä

Tässä tutkielmassa kuvataan kaasun ionisaatioon perustuvan korkean energiaerotuskyvyn hiukkasilmaisimen kehitystyö ja suunnitteluun vaikuttaneita tekijöitä. Kaasun ionisaatioon perustuva hiukkasilmaisin havaitsee ja mittaa hiukkasen liikeenergian keräämällä hiukkasen vapauttamat elektronit kaasusta sähkökentällä.

Työn tarkoituksena oli saavuttaa parempi energiaerotuskyky kuin mihin pii-ilmaisimilla päästään raskaille hiukkasille. Kaasuilmaisin toimii osana lentoaika-energia -spektrometria, jota käytetään Elastic Recoil Detection (ERD) mittauksiin. Energiailmaisimen parempi energiaerotuskyky tarkoittaa parempaa spektrometrin massaerotuskykyä.

Pii-ilmaisimet kärsivät lisäksi vaurioitumisesta hiukkaspommituksessa, mikä johtaa entistä huonompaan erotuskykyyn. Kaasun ionisaatioon perustuvat ilmaisimet ovat säteilynkestäviä ja kaasu voidaan aina tarvittaessa vaihtaa uuteen.

Jyväskylän yliopiston kiihdytinlaboratoriossa kehitetyssa ilmaisimessa on ohut itsekantava piinitridikalvo ikkunana, joka erottaa kaasun spektrometrissa muuten olevasta tyhjiöstä. Ikkunan paksuus ($\leq 100\,\mathrm{nm}$) on oleellista raskaiden rekyylien erotuskyvyn kannalta. Lisäksi tavoitteena oli saada ilmaisimesta paikkaherkkä, mikä mahdollistaa kinemaattisen korjauksen.

Kaasuilmaisin suunniteltiin ja rakennettiin onnistuneesti, ja sillä saavutettiin pii-ilmaisimeen nähden parempi massaresoluutio heliumia raskaammille rekyyleille verrattuna nykyisin käytössä olevaan spektrometriin, jossa energiailmaisimena on $450\,\mathrm{mm}^2$ Canberran PIPS pii-ilmaisin.

Contents

1 Introduction

Elastic Recoil Detection (ERD) is an ion beam analysis method for quantitative depth profiling of elemental composition in thin films. Originally ERD was done with just an energy detector in the forward direction and absorber foils to suppress incident beam [1] and was used for hydrogen detection in samples.

Today thin films of thickness 1-100 nm can be profiled typically with a resolution of nearly 1 nm at the surface. Using more energetic incident beam samples can be probed deeper, up to several µm [2], but often with reduced resolution. Heavy-Ion ERD (HI-ERD) with heavier projectiles like ^{35}Cl, ^{63}Cu, ^{79}Br, ^{127}I or even ^{197}Au can be used to obtain depth profiles of not only the lighter elements but of practically every element present in the samples, limited only by the mass or elemental resolution of the spectrometer.

ERD requires not only energy spectrometry but particle identification for full elemental analysis. The primary approaches to solve this problem are ΔE - E detectors [3, 4], time-of-flight energy spectrometers (TOF-E) [5], magnetic spectrometers [6, 7] and Bragg ionization chambers [8] or other pulse shape methods [9]. Out of the ion beam analysis methods ERDA is one of the more demanding in terms of detector design. There is a need for simultaneous measurements of two or more parameters of the recoiled particle such as its energy, energy loss, time of flight, recoil angle, or charge to mass ratio.

Low energy heavy ion incident beams have a definite advantage over high energy beams when it comes to depth profiling near the surface of the sample. Lower energy improves the obtained resolution with time-of-flight detectors. For a time-of-flight measurement to be able to distinguish recoils with different mass the energy of the particle needs to be measured. The relative energy resolution is decreased for smaller energy recoils which combined with problems of energy measurement of heavy recoils makes the mass separation more difficult. The capabilities of a time-of-flight system are therefore not fully utilized until a high resolution energy detector even for heavy recoils is introduced to the telescope. There still remains room for improvement in the method, for example in obtaining isotopic composition or improving sensitivity.

Pelletron laboratory at JYFL Accelerator Laboratory has a Pelletron 5SDH-2 1.7 MV tandem accelerator with an RF source for ^{4}He and sputtering source for heavy ions. ERDA measurements are most often carried out with 5.1–6.8 MeV ^{35}Cl and 6.8–10.2 MeV ^{79}Br beams. The $\approx$ 2 MV accelerators are widely available and are used for routine analysis of thin film samples, often for the semiconductor industry. Other methods such as Rutherford Backscattering Spectrometry (RBS) and Particle Induced X-ray Emission (PIXE) are used with 1-3 MeV ^{4}He or ^{1}H beam with these accelerators. Some low energy TOF-ERD setups are in use [10–12] and have shown their power in near surface depth profiling.

2 Interaction of energetic particles with matter

For the operation of a gas ionization chamber to be understood the basic principles of radiation-matter interaction need to be reviewed. The main focus will be on keV and MeV charged particles.

2.1 Particle energy loss

A charged particle will lose energy in a medium by several means. The main interaction between the particle and matter is via Coulomb force due to fields created by the particle and atoms of matter. Stopping is mostly due to inelastic collisions between the particle and bound electrons of the matter but also due to elastic collisions between nuclei. The latter effect will play a role at low energies, typically near 10 to 100 keV. The effect of nuclear stopping is small, typically under 1%, when the energy of the particle is above 200 keV/u [13]. Additionally there can be excitations and radiative losses like bremsstrahlung. *Stopping power* or *stopping force* is defined as

$$S(E) = -\frac{dE}{dx} = -\left(\frac{dE}{dx}_{\text{nuclear}} + \frac{dE}{dx}_{\text{electronic}}\right). \tag{1}$$

Here the total stopping force is written as a sum of the two main contributions.

The stopping force depends on the energy dramatically. Formulas and models have been deviced to model this behaviour with a lot of work undertaken since the early 1900s. One of the most used formulas for energetic particles is the Bethe-Bloch formula [14, 15]

$$-\frac{dE}{dx} = \frac{4\pi}{m_e c^2} \cdot \frac{nz^2}{\beta^2} \cdot \left(\frac{e^2}{4\pi\varepsilon_0}\right)^2 \cdot \left[\ln\left(\frac{2m_e c^2\beta^2}{I \cdot (1-\beta^2)}\right) - \beta^2\right], \tag{2}$$

where $\beta = \frac{v}{c}$, m_e mass of electron, n electron density of the matter, z charge state of the particle, ε_0 ionization energy ja c speed of light. What is relevant here is the $\frac{1}{v^2}$ dependence of stopping force to velocity of the particle.

For lower energies one needs to use other models. Often experimentalists rely on semiempirical models such as the one used in Stopping and Range of Ions in Matter

(SRIM) by J.F. Ziegler [16]. An example of the stopping force of ^{16}O in ^{28}Si given by SRIM is in figure 1. The stopping power of sufficiently energetic particles rises to a maximum known as the Bragg peak, named after William Henry Bragg who discovered the effect in 1903. The Bragg peak corresponds to a higher ionization right at the end of range for the particle, see figure 2.

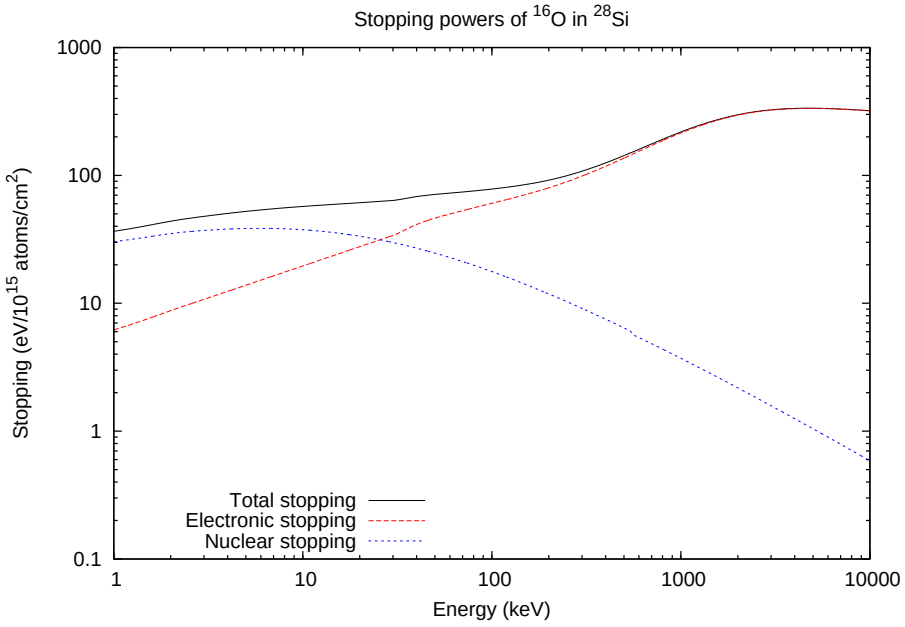

Figure 1: Nuclear and electronic stopping force of ^{28}Si for ^{16}O according to SRIM at energies between 10 keV and 10 MeV. The effect of nuclear stopping starts to be visible at energies below 1 MeV which corresponds to an energy per nucleon of 60 keV/u.

After particles have deposited their energy in matter they come to a stop. Stopping will therefore also determine the range of energetic particles in matter. The range can be found by evaluating the integral [17]

$$R = \int dx = \int_{E_0}^{0} \frac{dE}{(dE/dx)}. \tag{3}$$

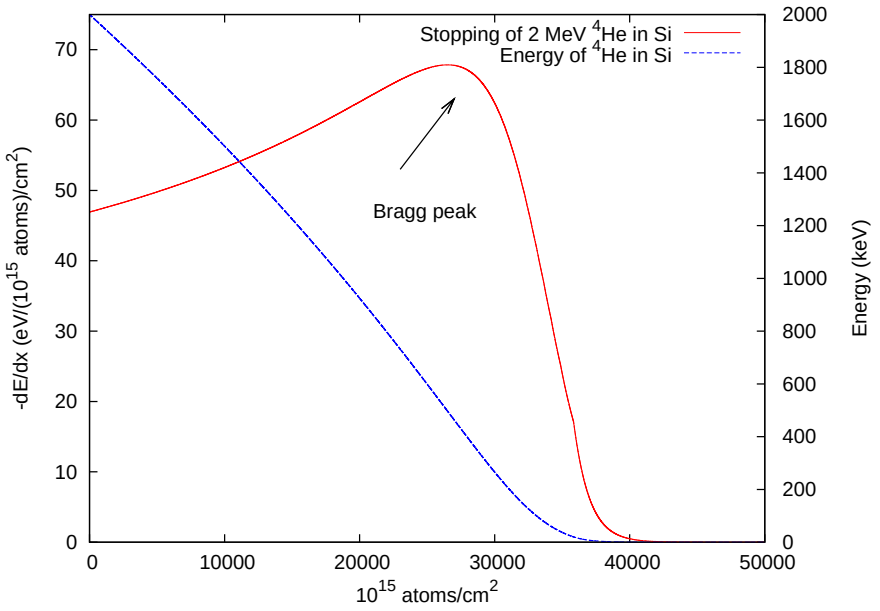

Figure 2: Stopping force and energy in natural Si for ^{4}He as a function of depth in sample. The ^{4}He incident particle has an energy of 2 MeV at the surface and it comes to end of range after the first $40\,000 \times 10^{15}$ atoms/cm^2 $\approx$ 8.0 µm. Data from SRIM.

2.2 Ionization

Most of the energy lost by a charged particle in a medium will result in ionization of the target matter. The ionization can be either primary ionization created directly by the incident particle or ionization by recoiling atoms of the target. For light ions most of the energy lost is transferred to primary ionization, for example 500 keV ^{1}H deposits $\approx$ 99.8% of its energy this way in isobutane gas according to TRIM-2010 simulation. This is noticeably different from the case with low energy heavy particles, 1 MeV ^{79}Br deposits only $\approx$ 34% by primary ionization and $\approx$ 39% by ionization via recoils in isobutane. This is due to increased recoil cross sections at low energies and larger nuclear stopping.

2.3 Straggling

A beam of particles slowing down in matter will introduce a spread in the beam energy known as straggling. Stopping process is a statistical phenomenon and therefore the energy of similar particles penetrating the same amount of matter will always have a slightly different energy afterwards. Straggling will eventually limit the energy and depth resolution of any ion beam analysis method.

The most used model for straggling is the Bohr theory, which assumes individual collisions between particles and target electrons transfer small amount of the total energy. This results in gaussian energy loss distribution [13].

At high energies electron excitations will introduce more straggling than predicted by Bohr theory. At low energies charge exchange and effective charge of the penetrating particle have to be taken into account. The latter corrections are introduced in the straggling models first by Chu [18] and Yang [19].

A spread of the ion tracks is also observed for particles, this is called lateral straggling when it occurs in a direction parallel to the direction of the beam or range straggling when it occurs in the same direction as the direction of the beam.

3 Gaseous detectors

Gas ionization chambers (GIC), ionization counters and other detectors that are used to detect radiation by means of measuring ionization are collectively known as gaseous detectors or simply gas detectors. Ionization chambers have been used since the early days of nuclear and particle physics to detect and measure ionizing particles [20]. First particle detectors such as the cloud chamber were impractical for most measurements. Having a device like an ionization chamber which can be used to detect radiation as an electrical signal was very useful.

Early gas ionization detector development was done in the 1940s and applied to nuclear reaction studies. The single most important task was alpha spectroscopy. Gas counters still find a role in the same field.

Gas detectors are nowadays very varied and are used to study radiation from a few keV X-rays to several GeV energies of some particles. There has been significant competition primarily from solid-state detectors, particularly silicon and germanium detectors. Particle physics experiments have used gas detectors mostly out of convenience as they are not damaged by highly energetic particles while providing suitable medium for deceleration. Modern experiments like CMS and ATLAS at CERN have shifted towards solid state silicon trackers and there has always been competition from scintillation detectors for high energy calorimeters. Still such detectors as Multi-Wire Proportional Chambers (MWPC), Drift Chambers, Time Projection Chambers (TPC) and MicroStrip Gas Chambers (MSGC) are used to measure the position of a particle [21] with good spatial and some temporal resolution. In this sense they are used as particle trackers. Most of these designs are absolutely unsuitable for low energy particle measurements, partially due to their complexity and design relying on the fact that measured particles are minimum ionizing particles (MIPs). Low energy ions would lose too much energy in the wrong places of the detector. The physics which these detectors rely upon does not always scale well. There has, however, been a lot of progress in this field of gas detectors, compared with the relative inactivity in gas detector development in other fields. There is something to be learned from the detector construction of particle physics experiments even though the ideas wouldn't be directly applicable.

3.1 Gas ionization chambers

Gas ionization chambers can be divided into three categories based on the strength of the electric field. When electric field is increased electron avalanches are created. In an ionization chamber no avalanches occur. In a proportional detector avalanches occur in a controlled manner allowing some energy resolution. In a Geiger-Müller (G-M) detector every sufficiently ionizing pulse of radiation gives a similar strong signal which cannot be used to deduce much information of incident radiation.

G-M detector can be used for counting purposes which is sufficient in beam monitoring or radiation safety applications [20]. Very simple electronics can be used and devices can be made hand-held and easy to use. Meanwhile the lowest detected gamma energy remains sufficiently small for radiation safety applications. The combination of these properties makes the Geiger-Müller counter an ubiquitous instrument, but the lack of energy resolution hinders its use in most scientific applications.

3.2 Detector physics

3.2.1 Ionization

As a particle ionizes gas inside the detector a certain number of molecules are ionized. Amount of ionization per unit length is proportional to the energy lost by the incident particle by a proportionality factor W and the total energy of the particle can be measured by allowing the particle to slow down completely in the active detection volume. The energy of the particle can therefore be expressed as

$$\bar{E} = W \cdot n_{\text{ion-electron pairs}}. \tag{4}$$

Ionization process is a statistical process, amount of ionization is not exactly similar for same energy particles every time, but there is a statistical variation. The process could be modelled as a Poisson process if there would be no correlation between ionizing events. However there is significant dependence, which reduces

observed variance. Each ionization event consists of a number of individual ionizing events and the energy lost in these events makes up the total energy loss to ionization. This constraint reduces fluctuations and improves resolution compared to a pure Poisson process [21, 22]. Relationality factor between observed variance on the amount of ionization and predicted variance by assuming a Poisson process is known as a Fano factor. The Fano factor is therefore typically expressed as

$$\sigma_{\text{observed}} = F \cdot \sigma_{\text{Poisson}}. \tag{5}$$

At low energies this model does not work very well due to the complicated stopping process [23]. Some of the primary energy is lost to ionization, some to kinetic energy of electrons, exitations of gas molecules and atoms which transform some of the energy to photons and Auger electrons and some of the energy is consumed by breakdown of gas molecules [23]. Statistical effects in ionization are important at low energies and choosing a gas with a small Fano factor and a small W-factor is suggested.

3.2.2 Charge collection and pulse formation

The resulting trail of liberated electrons and ions can be collected using a voltage, see schematic figure 3. If an electrode is biased with some voltage and another electrode is biased with a lower voltage, or is for example grounded, one can measure a pulse induced by the moving electrons and ions. The electrode from which the signal is measured is called the collecting electrode [24]. Due to ions and electrons having opposite charge they drift in opposite directions in the electric field. Electrons and ions eventually induce equal charge and therefore measurement of the total pulse will always result in a non-position sensitive signal. However electrons due to their orders of magnitude smaller mass drift much more quickly and induce a faster pulse. Ion-induced signal can be rejected by integrating the signal with a time constant sufficiently long to get the full electron signal but short enough to reject the ion induced signal. This condition can be expressed as

$$\Delta t^- \ll RC \ll \Delta t^+, \tag{6}$$

where Δt^- is the electron collection time, Δt^+ is the ion collection time and RC is the time-constant of the detector with resistance R of the signal plate of capacitance C to ground. By placing an AC-coupling capacitor and using a resistor to ground or some DC high voltage this RC constant can be tuned. However this is hardly practical and in practice filling the condition (6) might prove to be difficult as the resistor value R needs to be high to reduce leakage current. This device is called an electron-pulse chamber [24]. The fast pulse induced by electrons is not only proportional to the charge but to the potential difference of the point of ionization and collecting electrode [25]. This property can be exploited to achieve position sensitive detectors, but it also complicates energy measurement.

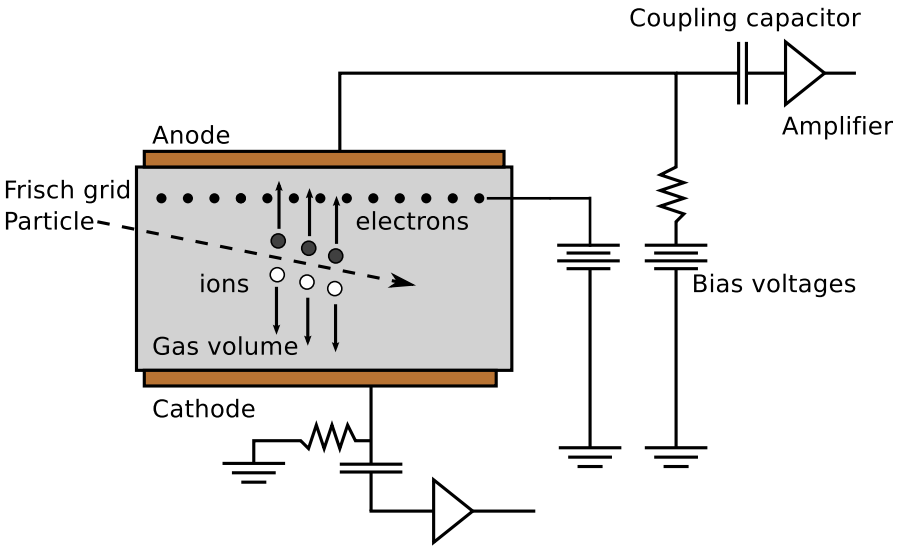

Figure 3: Schematical picture of a pulse-mode parallel plate ionization chamber where the anode is biased and cathode grounded. Preamplifiers are AC coupled.

It is possible to achieve a signal proportional directly to the energy of the particle by adding a grid of wires between electrodes which is biased to an appropriate voltage between the electrode voltages. The induced charge from the motion of electrons between one electrode and the grid is not induced to the other electrode, but as electrons pass through the grid a signal is induced. The grid therefore shields the collecting electrode. Now the potential difference of drifting charges seen by the shadowed electrode remains constant and signal does not depend on the point of ionization, but instead the full charge of ionization is collected. This grid is now

known as a *Frisch grid*, first implemented by Otto Frisch around 1940 [26]. It is used in high resolution detectors with few exceptions.

Electric field strength is important in several ways. If no or very small voltage is applied to the electrodes the opposite charges tend to recombine. Higher voltage will yield faster pulses which are typically preferred to achieve higher count rates and reduce electron-ion recombination [21]. At some high electric field drifting electrons will cause further ionization creating an effect known as electron multiplication or at even higher voltage an avalanche. If amount of electron multiplication can be predicted with some accuracy this feature can be exploited to have a better energy resolution due to smaller post-detector amplification. An unpredictable avalanche of electrons is also useful if one doesn't mind losing energy resolution. To ion beam analysis energy proportionality is a minimum requirement and operating in the avalanche region is unsought for. The highest obtainable energy resolution is possible only in the ionization region when both recombination and multiplication are minimized. Only at the lowest energies where electronics noise due to small amount of detected charges dominates there is an advantage of the gas amplification, like in the case of GEM detectors [27].

3.2.3 Geometry

This far we have only concerned ourselves with planar geometry where the entrance window is in a parallel plane with the electrodes. Alternatively the window could be in the same plane as the grid and electrodes, these detectors are either transmission detectors such as position sensitive detectors (PSD) or some form of a drift chamber. One very important geometry is the cylindrical detector which are often used often in avalanche mode. The avalanche occurs near central wire, which is chosen to be thin enough, typically between 20 and 100 µm diameter [21]. Due to the shape of the electric field its density is highest near the wire. Cylindrical ionization chambers do exist [28,29], in this case the wire is either thick or replaced by a tube or there are wires in intermediate potential to reduce field density near the anode and/or act as a Frisch grid. Cylindrical chambers also reject ion-induced signal when chamber is operated in the ionization chamber mode. This is due to logarithmic dependence on the distance of ionizing track to the signal induced on the anode. If the central wire diameter is assumed to be $\frac{1}{1000}$ of the cylinder diam-

eter and the particle ionizes equidistant from anode and cathode the ion-induced signal will be 10% of the electron-induced signal. A cylindrical ionization chamber is presented schematically in figure 4.

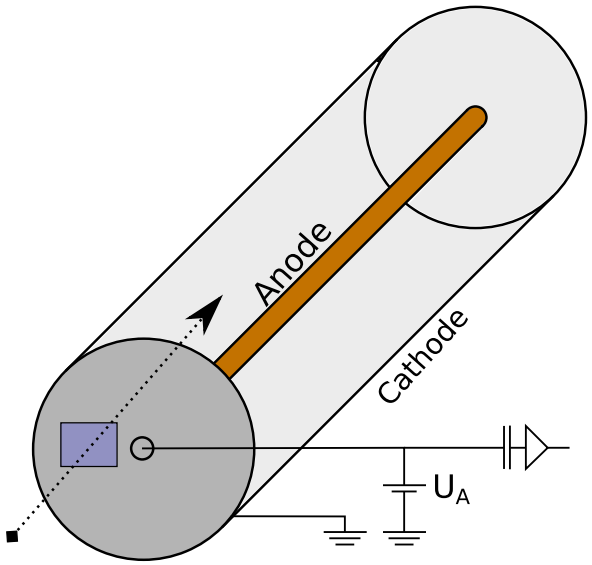

Figure 4: Schematical picture of a cylindrical ionization chamber where the anode wire is biased and cathode grounded. Particles enter through a small window at the end.

3.3 Gas and pressure

The choice of gas is not an obvious issue. The way the gas is chosen has been largely based on experiments with different gases. A good detecting gas for an ionization chamber most importantly needs to have a low ionization energy. This criteria is met by most gases, the ionization energies vary between 20 and 40 eV. Refer to section 3.2.1 on how the Fano factor is of signifigance to energy resolution. These two factors are most critical, but there is also something to be won by choosing a non-ideal gas, which is more dense than the ideal gas law would predict. These gases stop particles in a shother distance for a given pressure. An example of such gases are some organic gases such as isobutane or penthane. Heavy molecules will anyway be more dense in the same pressure as light molecules.

The motion of a cloud of electrons or ions in a gas volume with an electric field is thought to move with a constant velocity known as the drift velocity v_{D}. The drift velocity is often given as [21]

$$v_{\mathrm{D}}^{\pm} = \mu^{\pm} E \frac{p_0}{p}, \tag{7}$$

where p_0 is the standard pressure (1 atm), p pressure of the gas, E the electric field strength μ^+ and μ^- are the ion and electron mobility respectively. This equation is based on the fact that drift velocity is observed to be fairly linearly proportional to electric field and inversely proportional to pressure. In most cases this simple approximation is not exactly true, but in that case we have to consider the proportionality of μ to E and p. Often μ is assumed to be a constant, however.

In most cases a pure single molecule gas will be the best choice for the energy resolution, but a carefully selected mixture of two gases can be advantageous if electron mobility needs to be optimized. This is particularly true if noble gases or other low electron mobility gases are used as the primary gas. For example the electron mobility for Ar/isobutane 93/7% mixture is $25\,\mathrm{mm\,\mu s^{-1}}$ at electric field strength of $1\,\mathrm{kV/cm}$ and 62/38% mixture has much higher electron mobility of $50\,\mathrm{mm\,\mu s^{-1}}$ at the same field strength [21].

The nuclear energy loss and straggling of nuclear stopping affects resolution especially when low energy heavy ions are used. Nuclear stopping in the gas can be reduced by choosing a low Z gas. As both carbon and hydrogen have low Z this factor also supports the choice of methane, isobutane, penthane or a mixture of them as the working gas.

The matter of gas composition is very important in Geiger-Muller counters where one is not interested in the energy resolution but needs to control the avalanche process. A gas known as a quenching gas needs to be mixed in with the primary ionizing gas to stop the avalanche after the primary ionization process. This gas will need to slow down electrons so the electron multiplication with the primary gas will not continue for too long. This can be achieved alternatively by choosing appropriate R of the high voltage resistor, so that a high current pulse will momentarily reduce the voltage of the counter. Quenching gases are typically hydrocarbons while the working gas is often a noble gas such as argon or xenon.

The gas should be of high purity to avoid impurities which could promote electron attachment and recombination. For example the mean time between electron attachment in H_2O is 140 ns and in O_2 190 ns under normal conditions without electric field [21].

High pressure gas will also stop particles in a shorter distance, giving reduced straggling but higher ionization density. Large pressure can increase charge collection time by reducing drift velocities of the electrons and reduce the efficiency of charge collection via recombination. Higher electric field strength is needed to compensate this.

3.4 Entrance window

Straggling in the entrance window can be a major source of degradation of energy resolution. Some Geiger-Müller tubes use thin films of mica as windows. Typical choices for entrance window material in proportional counters and ionization chambers have been polymers, which can be made quite thin, even thinner than 1 µm. However thin polymer films such as Mylar (PET) will have pinholes which allow some of the detector gas to leak. The film is also very delicate and needs to be mounted on a supporting grid of wires. Some of the fluctuation in observed energy loss is also due to inhomogeneities of the film. Large surface areas are not a major problem and polymers are still important window materials.

3.4.1 Silicon nitride windows

A more modern choice is a self-supported silicon nitride (Si_3N_4) window [30, 31]. It does not leak detectably and it can be made as thin as 30 nm depending on the window size, pressure difference over the window and manufacturing process. A window of 100 nm thickness is mostly transparent for light ions at all energies, but some straggling will still contribute to the resolution of the detector, especially for low energy heavy ions. The thickness and uniformity of the entrance window are important [30] in order to achieve a good energy resolution. The thickness uniformity is more important than the ultimate low thickness [3]. Silicon nitride films are also very good in this respect.

Silicon nitride film is deposited on both sides of a silicon wafer using Low Pressure Chemical Vapor Deposition (LPCVD) from $SiCl_2H_2$ and NH_3 precursors. Windows are opened using for example Reactive Ion Etching (RIE) after which silicon is wet etched from the openings, see figure 5. The remaining silicon nitride membrane is self supporting and has low stress. These windows are available commercially for example from Silson Ltd [32] in standard sizes up to a size of as $5 \times 5\text{mm}^2$ and with thicknesses of 30, 50, 100 nm and thicker. The current (June 2011) price for a 100 nm thick $5 \times 5\text{mm}^2$ window is approximately 50 euros. Larger windows up to a size of $20 \times 20\text{mm}^2$ have been demonstrated. For detector purposes there is always the option of using a matrix of windows. The only problem are the etched borders, since the etching angle is only 55 degrees as determined by the silicon lattice. With low energy heavy ion beams these are almost insignificant as the amount of silicon needed to stop the particles is low. Still, some particles will traverse the silicon through the etched borders and are a source of energy straggling. One can install a carefully aligned collimator before the window to reduce this problem.

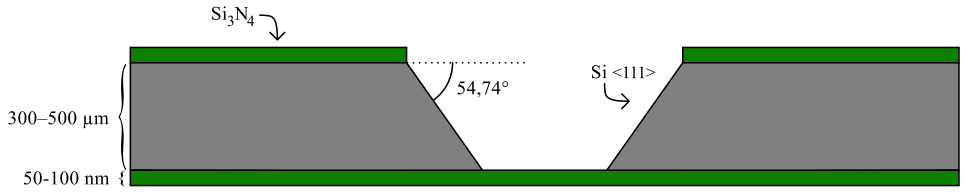

Figure 5: Cross section of a silicon wafer showing the etched shape.

3.5 Frisch grid

The Frisch grid has to shield the anode from the motion of electrons between the grid and the cathode. Otherwise the signal will have some position sensitivity which can not be easily corrected and will degrade energy resolution. The amount of signal passing through is known as Frisch grid inefficiency (FGI) defined as σ in equation 8. The actual measured anode pulse $P_{\mathrm{A}}^{\mathrm{measured}}$ can be written as [33]

$$P_{\mathrm{A}}^{\mathrm{measured}} = P_{\mathrm{A}}^{\mathrm{ideal}} + \sigma \times P_{\mathrm{C}}^{\mathrm{ideal}}, \tag{8}$$

where $P_{\mathrm{A}}^{\mathrm{ideal}}$ is the pulse induced to the anode with an ideal Frisch grid and $P_{\mathrm{C}}^{\mathrm{ideal}}$ the ideal pulse induced to the cathode. The FGI can be calculated from equations [34]

$$\sigma = \frac{l}{l+p}, \tag{9}$$

$$l = \frac{d}{2\pi}\left(\frac{1}{4}\rho^2 - \log(\rho)\right), \tag{10}$$

and

$$\rho = 2\pi\frac{r}{d}, \tag{11}$$

where r is the radius of wires, d is the grid pitch and p is the grid-anode distance. Typically the minimum of σ near $\frac{r}{d} = 0.23$ is used. The inefficiency as a function of $\frac{r}{d}$ for some combinations of p and d is plotted in figure 6. To obtain accurate value for the inefficiency of a particular grid it has to be measured [33]. Additionally grid has to be kept at a constant voltage and not allowed to fluctuate. This usually means that the grid is to be connected to ground through a capacitor.

The grid has to perform this function while it has to be as transparent to electrons as possible. If electrons are stopped in the grid the full energy is not measured, which reduces signal to noise ratio and introduces new statistical effects at low ionization. This is also connected to the geometry and the shape of the electric field near the grid wires. Grid is considered to be transparent to electrons if no electric field lines cross wires, except for the line passing exactly through the center of the wire. This approximation assumes that electrons follow electric field lines which is quite valid since electrons are not accelerated to large velocities. In other words electrons collide with gas molecules sufficiently often that we can consider their free path to be short in comparison with grid dimensions. The mean free path λ in most gases is in the order of 10^{-5} cm under standard conditions [21]. This means that even for low pressure gases ($\approx$ 10 mbar) the mean free path is approximately 10 µm. Therefore the path of the electron is mostly governed by the electric field and not by diffusion. Electric fields for a given geometry and potentials can now be solved using a Finite Element Method (FEM). In figure 7 is a FEM simulation of a Frisch grid showing equipotential lines. No lines cross the wires, which means the wire has a lower potential than its surroundings. The drifting electrons will therefore move around the wire and the grid is transparent.

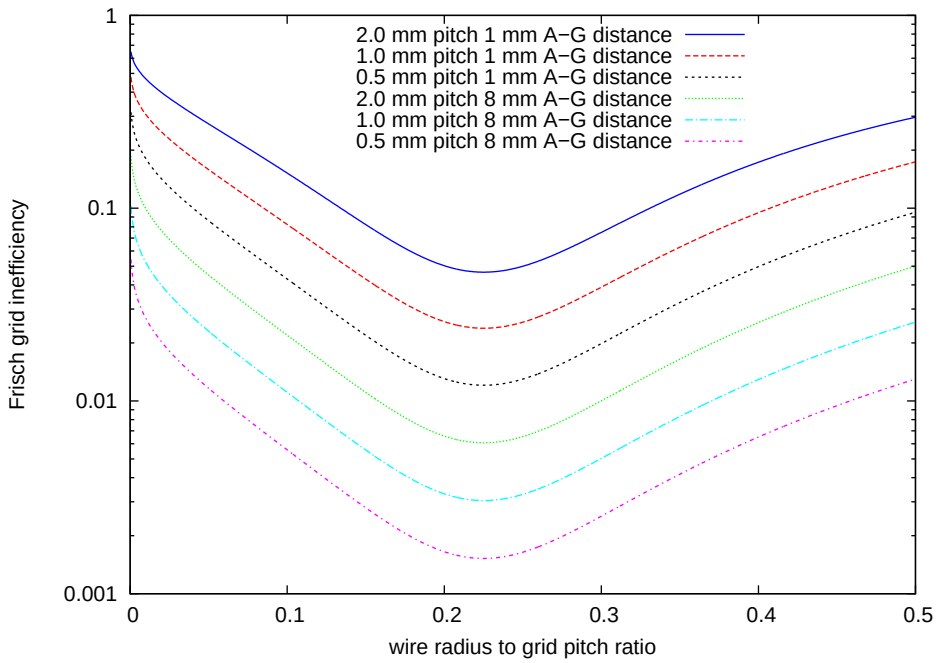

Figure 6: Grid inefficiency σ as a function of the ratio of wire radius to grid spacing for different combinations of grid anode-grid distance and wire spacing. Plotted using equation (9).

One could simulate the grid with programs such as SimION [35] which solve electric fields based on a given geometry and then simulate the motion of electrons in either two or three dimensions. The simulations especially in a three dimensional case are computationally intensive and extracting quantitative data from simulations would require plenty of information of collisions between electrons and gas molecules. Most of the currently available collision models for SimION are relatively simple and results should be correlated with actual measurements. Solving the problem of grid transparency therefore seems a bit too difficult a task for a quick SimION simulation. Qualitatively it is however seen that the behaviour of electrons in gas follows the general principles outlined above.

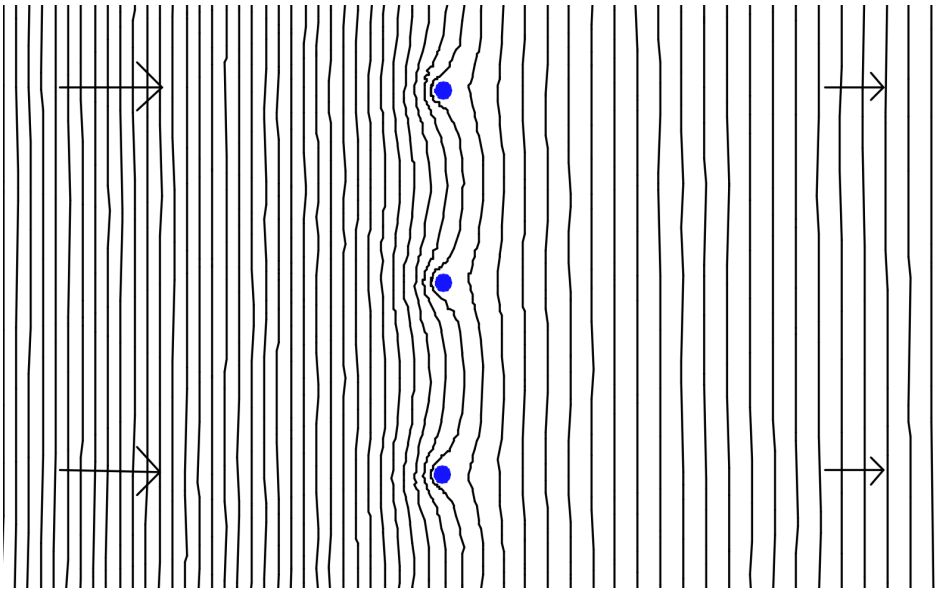

Figure 7: Two dimensional planar FEM simulation of a biased Frisch grid. Black lines are equipotential lines at 1 V intervals. Wires (in blue) are crosscut perpendicularly in this plane. Anode is on the left-hand side, not shown. Note higher electric field strength between the anode and the grid. Arrows show the electric field vectors, electrons move in the opposite direction.

3.6 Electronics noise

The capacitive plates of a detector act as an almost ideal current source, where the current is due to the charge q_s created via ionization in the gas. Output voltage from a gas ionization chamber is simply expressed as

$$V_\mathrm{o} = \frac{q_\mathrm{s}}{C_\mathrm{s}}, \tag{12}$$

where q_s is the ionization charge and C_s the capacitance of the detector. This means that taking some values of $q_\mathrm{s} = (5\,\mathrm{MeV}/26.3\,\mathrm{eV}) \cdot e \approx 200000e$ and $C_\mathrm{s} = \epsilon\frac{A}{d} \approx$ pF the output voltage is in mV range. If the detector is AC coupled the voltage after AC coupling with typical 1-10 nF coupling capacitor is in microvolt range. Additional problems are created if the capacitance does not stay constant. For this purpose one needs a charge-sensitive preamplifier (CSP), which is an inverting operational amplifier with large gain and feedback through a capacitor C_s. If the gain $G \gg C_\mathrm{s}/C$ we can assume the operation amplifier is ideal and the voltage

output is now

$$V_{\mathrm{o}} = \frac{q_{\mathrm{s}}}{C}. \tag{13}$$

This means the capacitance of the detector itself does not affect the amplitude of signal and the preamplifier acts as a charge integrator. The electronics noise consists of two independent contributions, shot noise and thermal noise. The source resistance and transresistance of the preamplifier create a contribution through white spectrum of thermal noise which is due to kT energy of the electrons. The other contribution, shot noise, is due to the charge q_{s} consisting of a finite number of electron charges. The standing currents at the preamplifier transistor fluctuate as the number of actual charge carriers change. Both types of noise need to be addressed, and typically noise is rejected by a band-pass filter which is combined with an amplifier. This device is known as a spectroscopy amplifier. The frequency at which the band-pass filter is centered is chosen with a shaping time τ. For a more complete discussion on electronics noise see ref. [36].

The noise of the whole chain of electronics is expressed as the RMS deviation of the detected charge. This number is typically gives as number of electrons and known as Equivalent Noise Charge (ENC). The noise proportional to $\sqrt{\tau}$ is known as parallel ENC and can be expressed as [36]

$$\mathrm{ENCP} = \frac{C_{\mathrm{s}} e}{G}\sqrt{\langle V^2\rangle_{\mathrm{P}}} \equiv e\sqrt{\tau\left(\frac{kT}{2R_{\mathrm{s}}} + \frac{qI_{\mathrm{B}}}{4}\right)}, \tag{14}$$

where e is the Euler's number, τ shaping time, I_{B} current through base resistance at the preamplifier or the drain current of a FET, q charge of the electron, R_{s} preamplifier source resistance and $\langle V^2\rangle_{\mathrm{P}}$ mean square voltage due to parallel noise at the output.

The series noise due to shot noise is proportional to $\sqrt{1/\tau}$ and given the transconductance g_{m} of the preamplifier transistor can be expressed as [36]

$$\mathrm{ENCS} = \frac{C_{\mathrm{s}} e}{G}\sqrt{\langle V^2\rangle_{\mathrm{S}}} \equiv eC_{\mathrm{s}}\sqrt{\frac{kT}{2g_{\mathrm{m}}\tau}}. \tag{15}$$

From equations (14) and (15) one can observe that the series noise will dominate as the detector capacitance increases, because the parallel noise is not dependent

on the capacitance at all. The transistor in the preamplifier itself acts as a source of series noise as well. Thermal noise proportional to $\sqrt{kT}$ is present in both contributions. This means cooling of the transistor of the preamplifier is beneficial as it reduces the thermal noise at the transistor and improves transconductance g_{m}, which futher reduces the series noise. Preamplifier RMS noise is given by the manufacturers as a function of input capacitance, see figure 8 for the noise FWHM as a function of input capacitance. This figure is easily reproduced if noise at zero capacitance, i.e. parallel noise, is given, it is 0.67 keV FWHM for silicon detectors at 2 µs shaping time, and if the noise slope (13 $\frac{\mathrm{eV}}{\mathrm{pF}}$) and capacitance (8 pF) of the preamplifier transistor are given. The series and parallel noises are statistically independent and can be summed quadratically

$$ENC = \sqrt{(ENCS)^2 + (ENCP)^2}. \tag{16}$$

The transistor capacitance C_t and the detector capacitance C_d can be summed to give the total source capacitance since they can be treated as parallel capacitances.

The reproduction of the original figure based on these values is given in figure 9, but this time the vertical axis corresponds to FWHM assuming $W = 26.3\,\mathrm{eV}$/electron-ion -pair. The vertical axis is therefore scaled by $\frac{26.3\,\mathrm{eV}}{3.63\,\mathrm{eV}}$. From this image it is clear that the electronics noise is already a significant source of error, considering this is a state-of-the-art preamplifier under ideal conditions. In reality these values are difficult to achieve and therefore represent theoretical minima. However, the effect of the input capacitance is fairly low in Amptek CoolFET preamplifier, and should the detector capacitance be higher there is an alternative FET with a higher capacitance, offering reduced noise slope. The drain current of the FET can also be increased by changing the drain current resistor to reduce noise slope by increasing transconductance. This will however increase the parallel noise due to thermal noise.

The performance of a preamplifier with a specific detector can be tested by connecting the detector to the input of the preamplifier and feeding pulses from a calibrated pulser. The test input is connected to the input of the FET of the preamplifier similarly to the actual input. Alternatively the detector can be replaced by connecting an equivalent capacitance at the preamplifier input. Measuring pulse height spectrum with an MCA and a spectroscopy amplifier will reveal the actual RMS due to electronics. This procedure relies heavily on a good and

calibrated pulser capable of producing pulses with the right rise and fall times, the lack of which prevented these measurements in this study.

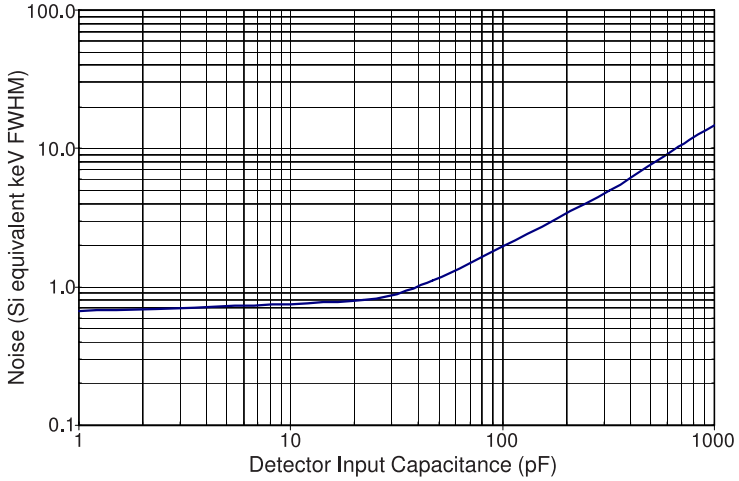

Figure 8: Noise (FWHM) of Amptek CoolFET peramplifier as Si detector response equivalent (W= 3.63 eV) as a function of the input capacitance when preamplifier is DC coupled, 1 keV of noise in Si detector (FWHM) is approximately 120 electrons RMS. The FET of this preamplifier is cooled, which makes the noise slope relatively gentle.

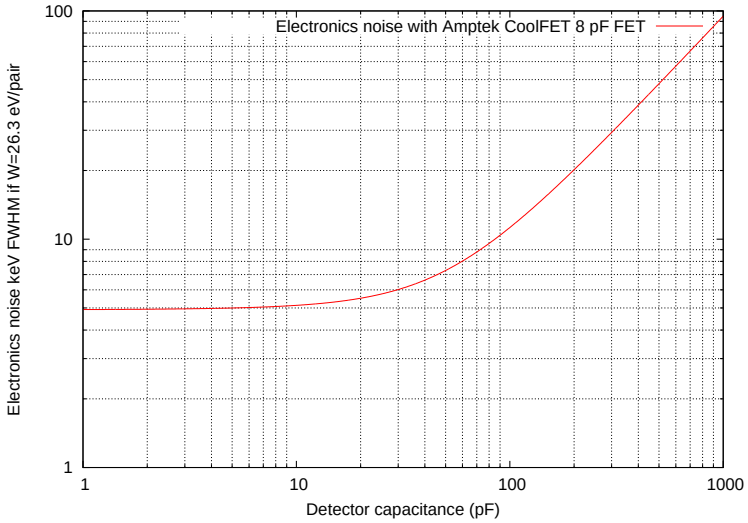

Figure 9: Amptek CoolFET RMS noise in keV FWHM as a function of the input capacitance, assuming W=26.3 eV/pair which corresponds to isobutane and values given for noise at zero capacitance and noise slope by the manufacturer.

3.7 Position sensitivity

Position sensitivity can be implemented in gas detectors using various techniques. Most techniques give one dimensional position information and combination of two different methods is typically used to achieve two dimensional position sensitivity.

Measuring pulses from an ungridded electrode to get a position and energy sensitive information and from a gridded electrode in coincidence is simple and doesn't affect energy resolution. Position in the anode-cathode direction is obtained, but this method is highly dependant on the shape of the electric field of the detector which is typically non-ideal, especially in planar electrode gas ionization chambers.

One major problem in these detectors is the position sensitivity due entrance window aberrations [38]. If the entrance window is at ground potential ionization in the first few millimeters of the active volume will not create ionization at the same potential as in the rest of the detector. Deeper inside the detector closer to ideal electric field is achieved, see also figure 10.

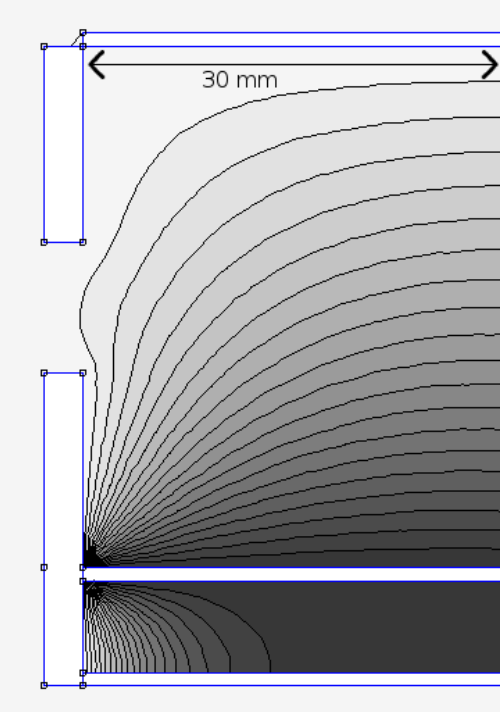

Figure 10: Two dimensional planar FEM simulation of fields near the entrance window in a plane perpendicular to the entrance window. The particles will enter the gas volume from the left. Frisch grid (middle) is simulated as a plane. Entrance window is left out of the simulation, i.e. it is assumed to have a permittivity of ϵ_0. Cathode (top) and the surroundings are assumed to be at ground potential. Entrance window aberrations are ample for this geometry but electrons should be collected from near the window even if Frisch grid does not start immediately after the window. The regions where the high electric field is strong, between the entrance window and the anode or the grid, should be void of free charges.

Another way is to split an electrode in two segments with a sawtooth-like pattern. Higher signal will now induce to the segment closer to the ionization trail. If one sums the signals the original energy signal is once again achieved. However using two independent chains of electronics will result in summing of noise. Some energy resolution will be lost if the split-electrode is the anode. It is also possible to measure energy signal from a separate grid between anode and Frisch grid, but this makes design more complicated. The advantage is that one does not need to split the anode to obtain energy signal. Splitting the cathode is also an obvious solution, but since particles create varying amount of ionization the resolution will be degraded in the other end of the position spectrum.

Third way to implement position sensitivity is timing. For example in a typical single grid detector where anode is shielded by the grid the charges drifting in the gas begin to induce a signal to the anode much later than in the cathode. Particles creating ionization near the grid will have short time difference between the cathode and anode signals but particles ionizing closer to the cathode will have longer time difference. Sources of error in measurement are similar to the pulse-height comparing methods but differ in one key respect – timing signals are mostly independent of the amount of ionization. Timing methods will yield a good linear behaviour but are the most complicated to set up.

All these methods have been used successfully. Typical resolution obtained varies between 1–5% depending on the method, implementation and solid angle of the detector.

4 Elastic Recoil Detection

Elastic recoil detection is used to analyze a sample by means of impinging an ion beam consisting of a single nuclide with well defined energy. Energy of the recoils of mass M_2 to an angle of ϕ with respect to the incident particle with mass M_1 and energy E_0 is

$$E_2 = E_0 \frac{4M_1M_2}{(M_1 + M_2)^2} \cos^2 \phi \tag{17}$$

when the incident particles have an energy of E_0 and mass M_1. In most measurements the ϕ is either assumed to be characteristic constant of the system or measured for each particle. The incident beam is kept the same, which fixes the value of M_1. However due to stopping of the incident particles the E_0 depends on in which depth in the sample the recoil originates from.

At the sample surface E_0 is known if the accelerator is calibrated correctly. This allows us to predict the energies of the high energy edges. Detected recoils will also have their energy reduced due to stopping in the sample. The distances particles will have to travel can be altered by tilting the sample in respect to the incident beam.

4.1 Time-of-flight ERD

A typical time-of-flight ERD telescope with two electrostatic mirror type timing detectors with MCPs and the measurement geometry is drawn schematically in figure 11. Measuring simply the energy or velocity distribution of the recoiled ions is not enough as one can see from figures 12(a) and 12(b). Different mass of recoils means that energy spectra of recoils have significant overlapping. Measuring both the time and energy in coincidence (figure 12(c)) will allow different masses to be separated, since

$$m = \frac{2E_\mathrm{k}}{v^2} = \frac{2E_\mathrm{k}}{\left(\frac{L}{t}\right)^2}. \tag{18}$$

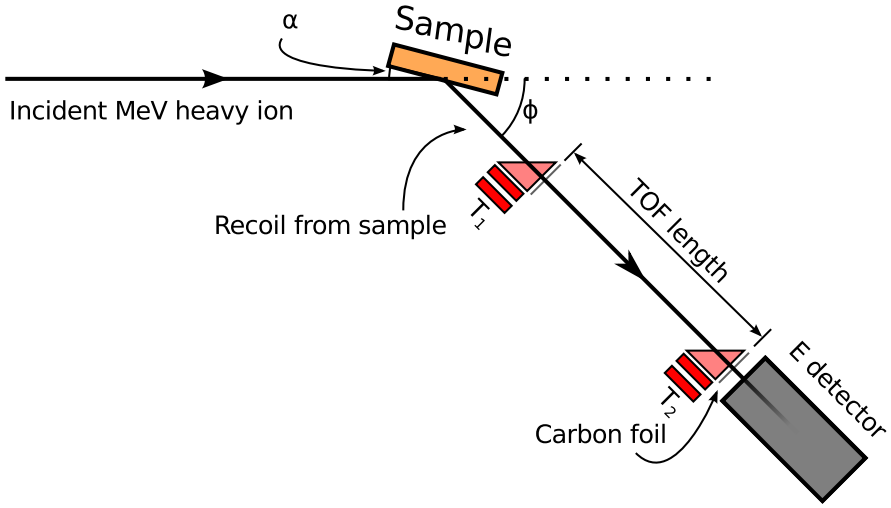

Figure 11: Schematical picture of TOF-ERD telescope and measurement setup geometry when sample surface is tilted to an angle of α with respect to the incident beam. The scattered incident beam and recoils are measured with the telescope at an angle of ϕ with respect to the incident beam. Time of flight is measured between the timing detectors T_1 and T_2 and energy of the particle with an energy detector, which can be either a silicon detector or a GIC. The particle is stopped in the energy detector.

The mass resolution can be defined as

$$\frac{\delta m}{m} = \sqrt{\underbrace{\left(\frac{\delta E}{E}\right)^2}_{\text{E detector}} + \underbrace{\left(\frac{2\delta L}{L}\right)^2 + \left(\frac{2\delta t}{t}\right)^2}_{\text{TOF detector}}}. \tag{19}$$

Time of flight measurement is mostly independent of the species of the incident particle and highly linear. The biggest contribution to the resolution is a simple constant error δt coming from MCP timing properties and amplification and timing electronics (CFD, TDC). The δt is typically between $\approx 100-1000$ps. Relative error is highest for the most energetic particles because of $\frac{\delta t}{t}$ term in it. This is in a stark contrast with a gas detector or a silicon detector which have the lowest relative error for energetic particles. It is therefore possible that highest energy resolution is obtained with the energy detector for high-energy light particles. However the very reliable energy calibration and worse resolution of the energy detector for most particles tends to keep the TOF measurement as the preferred method for energy measurement.

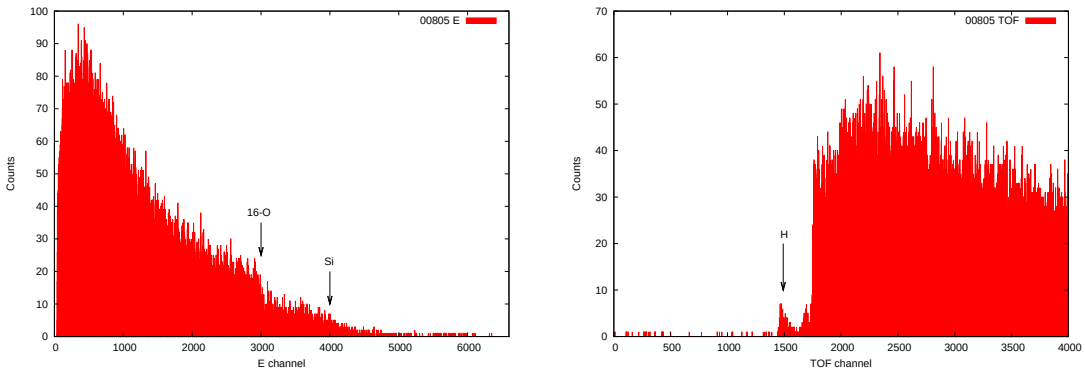

(a) (b)

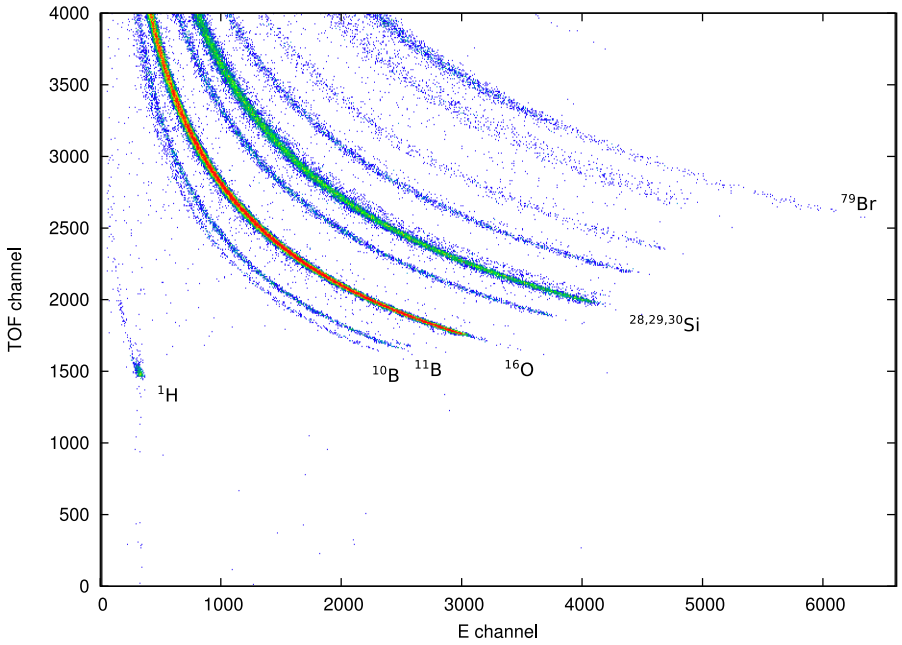

(c)

Figure 12: Histograms of TOF-E data measured in coincidence. Individual measurement itself does not give very much useful information. The energy measurement histogram in figure (a) consists of overlapping energy spectra of the different recoils. High energy edge corresponds to the energy of incident beam scattering from some heavy element present in the sample. Other front edges can be seen as knees which can be identified if the energy detector is well calibrated or against a reference sample. From the time-of-flight measurement spectrum of counts during first 250 ns of the 500 ns timing window are shown in (b). The surface peak of hydrogen can be resolved, but other recoils overlap. The power of a coincidence measurement is how different masses are separated into different "banana" curves in figure (c), where intensity of the 2D histogram is represented on a logarithmic scale.

4.2 Kinematic correction

Position sensitivity in scattering plane allows one to implement a simple first-order correction to tackle the problem of a finite detector size. In most experiments scattering is considered to occur in a fixed scattering angle but a large detector will naturally detect particles scattered to a range of scattering angles. Recoils to smaller scattering angles will be more energetic than the ones to a larger scattering angle as one can see from equation (17).

If straggling, multiple and plural scattering, and variations in the distance the recoils travel in the sample are neglected the observed energy of the particle corresponds to a certain depth in the sample for a constant scattering angle. Now when particles are measured scattering to a certain angle we can correct the energy signal, so that it corresponds to an energy at the centerline scattering angle. The result should be that energy signal corresponds to a single depth no matter what scattering angle the particle is detected. The whole process is done as a linear correction, which is not accurate for extremely large solid angles. However the results are improved greatly comparing to a situation where detector solid angle is simply approximated to be infinitely small.

It is also possible to calculate the true scattering angle from the position and use that result in the analysis.

5 The GIC built at JYFL Pelletron lab

As an experimental part of this thesis a gridded planar geometry pulse-mode GIC with a SiN entrance window was built. The detector was built to be mostly a proof-of-concept but it is usable for some measurements, only limited by its relatively small solid angle due to a small entrance window. It is possible to upgrade the current detector by installing a larger window, at least $15 \times 15\,\mathrm{mm}^2$ should be possible without other modifications to the detector. Mass resolution is slightly worse than that obtained with a Si-detector for hydrogen, but already noticably better for ^{10}B at all energies. Mass resolution is good enough to separate even isotopes of silicon at higher energies, like with 10 MeV ^{79}Br incident beam. Resolving ^{10}B from ^{11}B or ^{11}B from ^{12}C is possible even for very low energy measurements such as 3 MeV ^{35}Cl incident beam.

5.1 Dimensions of the detector

A GIC for TOF-ERD has to be custom designed to suit the needs of a particular TOF-setup. The energy range of measurement affects the range of ions in the gas and that sets some geometrical constraints on the design. Maximum gas pressure, entrance window thickness and detector geometry are all connected and much of the design is set by attempting to optimize these parameters while keeping in mind practical limitations.

There is not much generic data available of the pressure difference a silicon nitride window can withstand as it depends on the manufacturing process of the silicon nitride membrane. For the Silson Ltd manufactured $5 \times 5\,\mathrm{mm}^2$ windows 100 nm is enough to hold 200 mbar of pressure reliably, even a 50 nm window will hold 100 mbar [37]. A pressure of 100 mbar was the highest pressure these windows were tested with in Jyväskylä. Two 50 nm windows were also tested, the first one was accidentally destroyed when glued to the window assembly and the other one was destroyed by repeated pressure changes from vacuum to atmospheric pressure or some other mechanical stress. It was decided based on the data from windows made by Silson Ltd that 100 mbar should be the highest pressure used in the detector ever.

The length of the active gas volume sets the maximum range detected particles can have. The length of the anode will also increase the anode surface area and therefore the detector capacitance and lateral straggling of the particles should also be kept in mind. The anode can be cut if needed, so it was decided to have the longest possible electrodes there is space for. This was 250 mm. Some more room is required by an optional silicon detector which was used during the development to detect e.g. particles not stopped in the gas.

Lateral dimensions were constrained by two choices. The biggest constraint was that the detector was designed to be mountable either with anode/cathode plain parallel or perpendicular to the scattering plane. This symmetry requires that the active anode width is the same as anode-grid distance. The other limitation was that the planar electrodes would have to fit in a round tube, which was easiest to manufacture. Shoe-box style chambers are much more expensive and demanding to manufacture. The active width and anode-grid distance was set at 40 mm due to the limitations when 8 mm was reserved for the grid-anode distance, which was set by Frisch grid design.

5.1.1 Range of recoils and scattered beam

The range of different recoils depends on their energy and stopping. Stopping can be estimated for the highest energy recoils which have an energy given by formula 17. In figure 5.1.1 the tracks of particles with maximum energy given by 10.2 MeV ^{79}Br and 8.5 MeV ^{35}Cl incident beam for 41 degree recoil angle in 20 mbar isobutane are simulated with SRIM. The increased energy of the heavier recoils is opposed by the increased stopping power. The range of the particles of interest recoiling from the surface is fairly similar for ^{79}Br. For a lighter incident particle such as ^{35}Cl the lightest elements have the longest range.

The calculated ranges in 20 mbar of isobutane are all under 150 mm with less than 10 mm FWHM of lateral straggling. This 10 mm margin means entrance the side of the window needs to be 20 mm shorter than the grid-cathode distance. Additional reduction is necessary to compensate for the geometric effects. As long as entrance window effects are not of interest the range of particles can be tuned by increasing the pressure. Allowing particles to stop just before the end of the anode

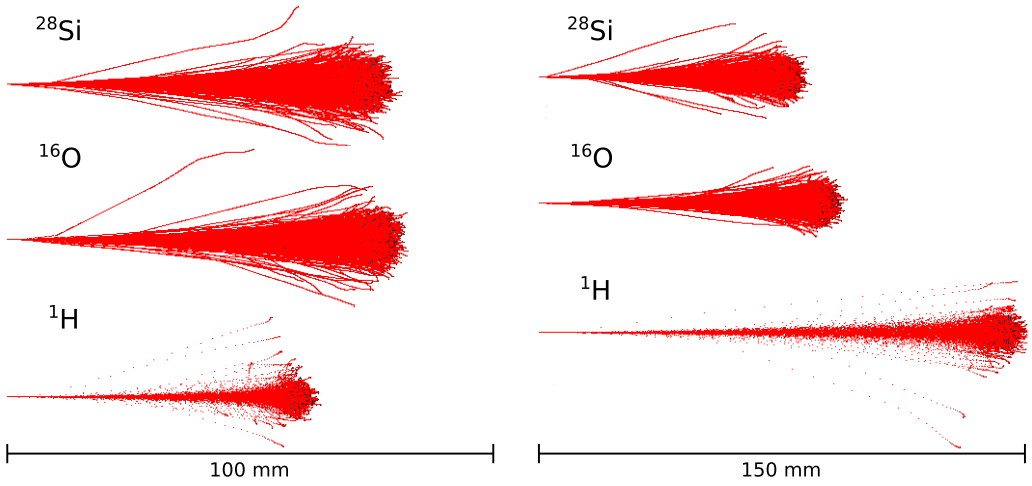

(a) (b)

Figure 13: Tracks of 1000 particles per nuclide and the resulting recoils in 20 mbar of isobutane simulated with SRIM. The particles have an energy corresponding to the maximum energy allowed by kinematics to a recoil angle of 41 degrees. In figure (a) the incident beam is assumed to be 10.2 MeV ^{79}Br and the recoils are ^{1}H (300 keV), ^{16}O (3400 keV) and ^{28}Si (4600 keV). The range of different recoils is quite similar, but there is a difference in lateral straggling. In figure (b) the incident beam is assumed to be 8.5 MeV ^{35}Cl and the recoils are ^{1}H (530 keV), ^{16}O (4170 keV) and ^{28}Si (4780 keV). The range of hydrogen for this beam is clearly the longest. Note the difference in scale between the figures.

is not possible due to too much lateral straggling for these particles if the window is too large. To take full use of the length of the anode a window of $15 \times 15\,\mathrm{mm}^2$ might be a reasonable compromise. Reducing the length of the anode would reduce capacitance and use of higher pressure would reduce lateral straggling and allow a larger window. This is the preferred option if large and thin windows capable of holding adequate amount of pressure are available.

In figure 14 the effect of having too little pressure to stop particles can be seen. A 6.3 MeV ^{35}Cl beam was used to measure recoiled oxygen from a sample with a thin oxide at the surface. Using 20 mbar of pressure all of the recoils of oxygen are stopped in the gas and a good energy resolution is achieved. With the 2 mbar and 3 mbar all of the recoils pass through the gas and a δE is measured, with the 3 mbar already much of the energy of the particles is measured. The highest energy corresponds to 3090 keV.

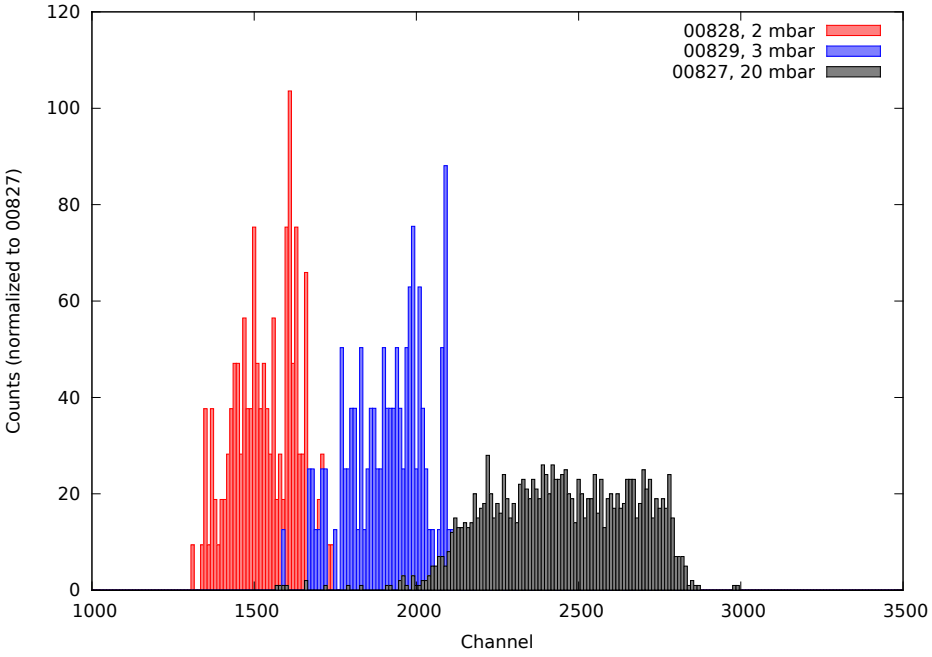

Figure 14: The effect of gas pressure to the measured pulse height spectrum from the anode. The spectrum is of oxygen recoiling from a thin oxide film, the highest energy corresponds to 3090 keV. With the 20 mbar pressure the recoils are stopped in the gas but not with the 2 or 3 mbar. Approximately 10 mbar would already be enough to stop these particles.

5.2 Vacuum and mechanical design

Just like in any other vacuum system vacuum design is of great importance. The MCPs of the timing gates set further requirements on the vacuum. The vacuum around the timing gates should be high vacuum, preferably in low 10^{-7} mbar range. To achieve this some care was put into design to avoid unpumped volumes and connecting vacuum volumes with large cross sectional area.

The GIC connects to the existing vacuum using two CF (ConFlat) flanges with copper gaskets: a CF100 (ConFlat) flange for mounting the detector itself to the rest of the telescope and a CF16 flange and a VAT UHV-compatible valve between the gas volume and high vacuum. Elsewhere ISO-K 160 and KF16 flanges are used as this facilitates quick reassembly.

The window assembly is attached using a custom fluorocarbon (Viton) gasket to the detector. This piece is critical to the vacuum design as it separates the detector

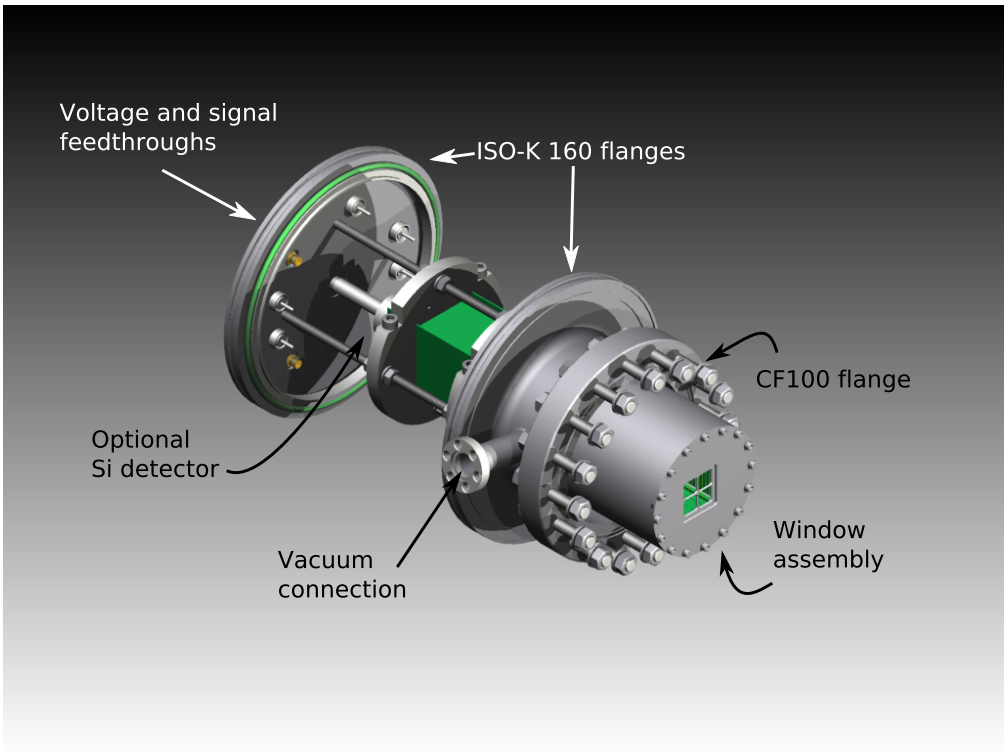

Figure 15: Mechanical construction of the developed GIC.

gas volume from the high vacuum present elsewhere in the detector telescope. The pressure difference between the detector volume and high vacuum will tend to push the window assembly outwards. The windows assembly has 16 M3 screws to ensure an even and a tight fit, but in reality 8 screws was more than enough. Weldments obviously need to be done with regular vacuum weld techniques. Material choices were mostly unaffected, although the use of epoxy is not recommended as this will increase pumping time significantly. There are alternatives to regular epoxy such as Varian Torr Seal, which is good for pressure as low as 1×10^{-9} mbar.

However in everyday use the gas handling turned out to be easy. When the detector is first installed some pumping time should be allowed. As the pressure decreases the detector is ready for the gas. The valve connecting the detector gas volume to the vacuum is closed. When some gas is now introduced to the detector extremely carefully one can observe the status of the entrance window indirectly by observing the pressure of the vacuum. If there is no change the window is intact and will hold more pressure. Pressure can be carefully increased to final pressure. When measurements are over the gas can be rough-pumped away, time-of-flight detector

high voltage is turned off and the valve to the gas volume can be opened gently. The remaining pressure is still high enough to trigger vacuum interlocks if care is not taken. Repeating the gas handling procedure is only necessary about once per day, and only takes a minute or two. The gas handling is the only increased effort from users point of view when comparing to a solid-state detector.

5.3 Electronics

The electronics of the detector consist of an AC-coupled preamplifier connected to the anode and a typical spectroscopy setup: a spectroscopy amplifier for pulse shaping and a multi-channel analyzer which converts the shaped pulse height into a digital value, see figure 16. Another preamplifier is connected to the cathode, this one is used to achieve position sensitivity in lateral direction. This preamplifier is also AC-coupled.

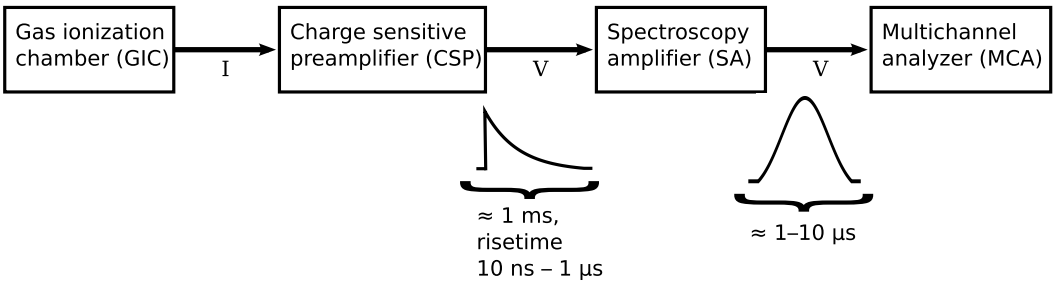

Figure 16: Typical spectroscopy setup for different detectors.

5.3.1 Preamplifier

Several preamplifiers were tested. Energy resolution for low energy particles is mostly limited by the electronic noise contribution, which makes the choice of preamplifier very critical. Originally relatively low noise, sensitive, low footprint and affordable Cremat CR-110 preamplifiers were tested. They were supposed to be mounted inside the gas volume, which has been done with good results [23, 37]. Preamplifier close to the source of the pulse reduces cable lengths which reduces

electronics noise by avoiding stray capacitance and EM pickup. The development of the detector with custom electronics is a demanding task, so the idea was abandoned for now. Self-made PCB boards with CR-110 preamplifiers proved relatively successful, noise performance was on par with factory assembled Cremat preamplifiers.

Further improvement was sought with an Amptek CoolFET preamplifier, the noise performance of which is state-of-the-art due to a Peltier-cooled field effect transistor. Cooling of the FET reduces thermal noise and improves the transconductance of the FET. The low frequency noise of the detector proved to be a problem with both the CR-110 and CoolFET with a protection diode installed. This noise is present as a difference in the DC level between two pulses in figure 17. The best performance was achieved with Ortec 142 -series preamplifiers, with both 142A and 142B achieving nearly identical noise performance. The 142A is intended for lower capacitance detectors and has higher conversion gain, which is an advantage since measured pulses are small. Since all tested preamplifiers have a similar operating principle and only small variations in implementation there is no reason why the best possible performance with example the CoolFET could not be utilized after some of the noise and possible oscillations in the preamplifier are eliminated. See examples in section 3.6 for noise performance of the CoolFET preamplifier under ideal conditions.

Preamplifiers were AC-connected, which means there is a capacitor separating the high voltage from the preamplifier. The capacitor is large enough not to increase the input capacitance of the preamplifier which is connected in series with the coupling capacitor. This preamplifier could also be DC-connected, but AC-connected preamplifiers are not as easily destroyed, since constant leakage current does not flow to the FET of the preamplifier. To achieve ultimately low electronic noise DC-connected preamplifier is essential. That is why the anode could be grounded and cathode and Frisch grid biased to a negative voltage. Positive voltage biasing has its advantages though, having everything above ground potential will suppress electron emission from surfaces and guarantee the collection of electrons. With negative bias voltages it is possible that some electrons are lost to the window assembly and are not collected by the anode [38].

When using the preamplifier it should be kept in mind that gas can allow dis-

charges even at moderate voltages that can damage the FET of the preamplifier easily. Solid state detectors are generally much more robust, since no large currents can flow through them. Some preamplifiers might have a protection network consisting of a current-limiting resistor at the input and back-to-back diodes connected to ground. Some designs do not have a protection diode in the forward-biased direction, since this configuration adds considerable noise from leakage current. In this case the protection diode should be designed to fail by latching closed before the FET is damaged, however damage to the this kind of protection diode is not recoverable. The diode can also be a bipolar junction transistor with collector and base shorted like in Ortec 142s or a FET with the gate and drain shorted as is the case in PAD1 protection diode found in the Amptek CoolFET preamplifier. Any protection network needs to be disabled for ultimate electronics performance due to stray capacitance and leakage currents.

5.3.2 Pulse shaping

Ordinary NIM-electronics spectroscopy chain of spectroscopic amplifiers and ADCs is adequate for further pulse processing. The detector was first used with Ortec 571 spectroscopy amplifier which has a single differentiating circuit and three integrating steps with pole zero -compensation. However noise performance due to low frequency noise on the preamplifier output was improved by using a Princeton Gamma-Tech (PGT) spectroscopy amplifier PGT 347 which is originally intended to be used with X-ray detectors. The operation principle of a spectroscopy amplifier does not depend on the type of detector, but it is presumed that the spectroscopy amplifier has circuitry to eliminate low frequency noise more efficiently than the Ortec amplifier. One can also filter this noise before the spectroscopy amplifier using high-pass RC-filters [39].

Another concern with spectroscopy amplifiers is the appropriate shaping time. Optimization of shaping time is crucial for reducing noise and thereby obtaining the best energy resolution. Since low frequency noise proved to be a problem long shaping times were out of the question. However long electron drift times ($\approx 1\,\mu s$) necessitate a shaping time of around $2\,\mu s$ in order to avoid ballistic deficit. NIM electronics that were available didn't support continously adjustable shaping time, so fixed values of either $2\,\mu s$ or $3\,\mu s$ were mostly used.

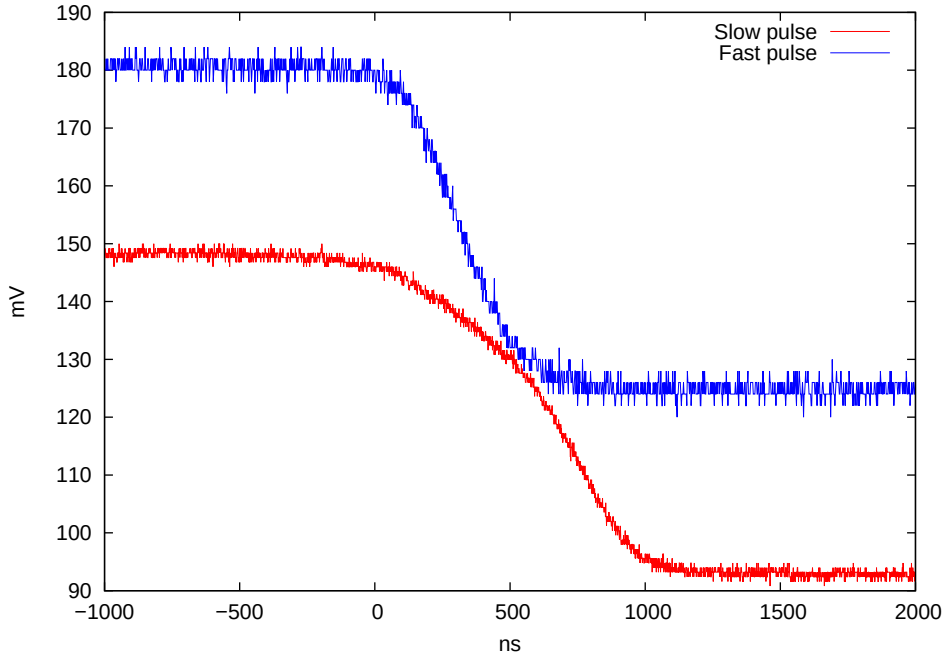

Figure 17: An example of two falling pulses from preamplifier output signal observed with a oscilloscope. The rise time of the preamplifier in ideal conditions is $\approx 50\,\text{ns}$. These two have slower rise time due to the long drift time of charges. Voltage pulse height ($\approx 50\,\text{mV}$) is the same as these events are from the same α source $E_\alpha \approx 5.5\,\text{MeV}$. The difference in absolute position is due to low frequency noise in the preamplifier output.

Under ideal conditions in a test bench it was observed that longer shaping times did not degrade energy resolution. This seems to support the evidence that low frequency noise is due to mechanical vibrations from the surroundings. Possible sources of high frequency noise are mostly external EM interference, which is eliminated via shielding by the metallic shell and avoiding long cables.

5.3.3 Anode, cathode and grid voltages

Collecting voltage to the anode and a grid voltage was obtained from a high voltage supply. Several power supplies were tested as well as a system based on 9 V batteries connected into series. Some high voltage supplies had more noise in

the output than others, even when connected similarly. Voltage to the anode was always supplied through the AC coupled preamplifier circuits, which have one or more RC-filters to filter out noise from the high voltage supplies.

To the grid voltage some filtering was done, first with just a 10 nF capacitor connecting the grid to the ground potential which ideally passes high frequency signals and leaves the grid at steady DC voltage. However a series resistor of 20 MΩ was added later and actually this RC filter did a better job of filtering the noise. The battery-based solution is of course the one that does not suffer from ground loops or high frequency noise and was used as a reference. The battery system was designed to deliver 450 volts which was used as the anode voltage, the grid voltage was obtained from the same source using voltage division with MΩ resistors. The cathode was always connected directly to ground.

The influence of the grid voltage and the anode voltage to the preamplifier pulse shape was studied with 5.5 MeV alpha particles at 70 mbar pressure. The ratio of anode and grid bias voltages was kept nearly constant at $\frac{V_{\text{anode}}}{V_{\text{grid}}} \approx \frac{3}{2}$ which corresponds to a ratio of $\approx \frac{5}{2}$ in electric field strength between the anode-grid and grid-cathode fields. The rise times are plotted as a function of the anode voltage in figure 18. The Amptek CoolFET preamplifier used has a short rise time, 2.5 ns at zero capacitance, and so the difference in rise times is mostly due to the actual drift velocity of electrons. The grid voltage was also varied when the anode voltage was kept constant and vice versa. The signal will be longer due to slower collection of charges if the anode or the grid voltage is decreased. The anode voltage has a stronger influence, since the signal is induced while the charges move between the grid and the anode. Too low grid voltage will also increase the rise time due to the charge pulse broadening in time domain. The shortest achieved rise time in this measurement was approximately 1 µs, which was achieved with anode voltages above 100 V and grid voltages above 50 V, but 30 V below the anode voltage.

At lower pressures the voltage required to have the same rise time will be lower. With measurements at 20 mbar no deterioration in energy resolution or timing properties were observed when running with 30 V of anode voltage and 20 V of grid voltage.

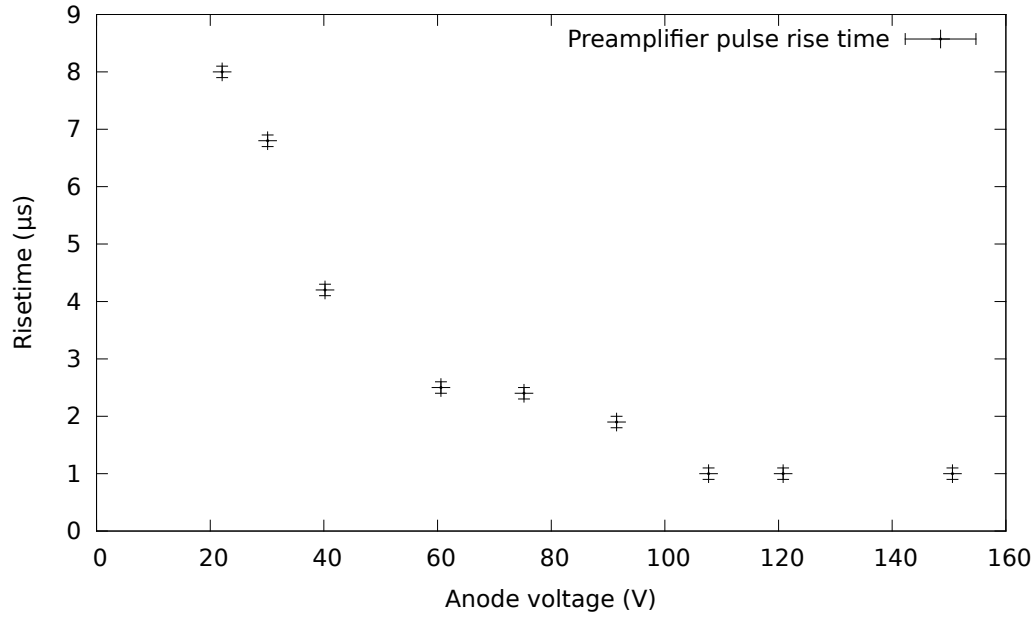

Figure 18: Rise time of preamplifier pulses as a function of anode voltage at 70 mbar of pressure for 5.5 MeV alpha particles. The ratio of grid and anode bias voltages was kept constant at $\frac{V_{\text{anode}}}{V_{\text{grid}}} \approx \frac{3}{2}$. The high voltage supply might have a large unknown uncertainty in the voltage reading.

5.4 Frisch grid design and manufacturing

The Frisch grid of the detector was implemented as a grid of 50 µm diameter parallel wires with 0.5 mm wire pitch on a milled circuit board support. These dimensions were set using methods described in section 3.5. The anode-grid distance was designed to be as small as possible, due to limited space. As the wire pitch needs to be small in comparison with this distance the wire pitch was chosen to be as small as practically possible. The wire pitch was originally designed to be approximately 1 mm, but since 50 µm diameter copper wire was available affordably it was decided to have a 0.5 mm wire pitch which is more optimal given the wire diameter. The calculated grid inefficiency is $\approx 1.2\%$. Smaller grid pitch would be better for this wire, but the manufacturing becomes extremely difficult. The grid-anode distance could now be of course reduced by several millimeters, but it did not seem wise to attempt to optimize the process before the construction of the grid was attempted, since is was known it could prove difficult, which it did.

As these grids are not commercially available it was necessary to build it in-house.

Wires were spun on top of a copperized circuit board using a custom made aluminium mount with the help of threaded rods. Wires were spun perpendicular to the direction of detected particles. Copper wire was chosen as it was the most economical and no issues were expected due to the wires being oxidised. Tungsten wires or gold plated tungsten wires are of course the best choice since they have higher tensile strength. But already at 50 µm diameter even pure copper wire proved to be adequately strong.

Threaded rods have a standard metric M3 thread, which means they have 0.5 mm pitch and 3 mm outer diameter. Other wire pitches require different threads. The process of spinning the wires will be more difficult with thinner rods, but threaded rods are also available in finer pitches. Wires should excert enough force on the circuit board to create a stable grid even under gravity and electrostatic forces [21]. The tension is limited by the supporting circuit board, material of the wires and the process of making the grid.

The circuit board is carefully attached to the aluminium support. Any deformations in the circuit board are not welcome, since these have an effect on the pull of individual wires and could result in some wires being loose.

After wires are spun they are glued on the circuit board using epoxy. It is critical that wires are in good contact with the copper surface at this stage, otherwise electrical contant between the wires and the circuit board could be compromised. Easiest way to be sure the contact is good is to use conductive epoxy which is commercially available or solder the wires in stead of gluing. Conductive epoxy contains enough silver particles to conduct electricity but still retains most of the mechanical properties of epoxy. After epoxy has dried wires can be cut.

This process however did not yield good grids since most of the wires were loose. The 500 rounds of copper wire will always excert force on the circuit board unevenly. The tension of wires was improved by supporting the grid to the anode using plastic blocks. These insulating blocks wrap around the anode and are attached to the sides of the grid using instant glue or epoxy. The block is compressed immediately after glue is applied, and held compressed until the glue has dried. After compression is removed the plastic block relaxes and spreads the grid tightening the wires. One block is enough to tighten wires in a few centimeters area, so

several are needed for this 250 mm long grid. A photograph of a grid manufactured using this process is in figure 19.

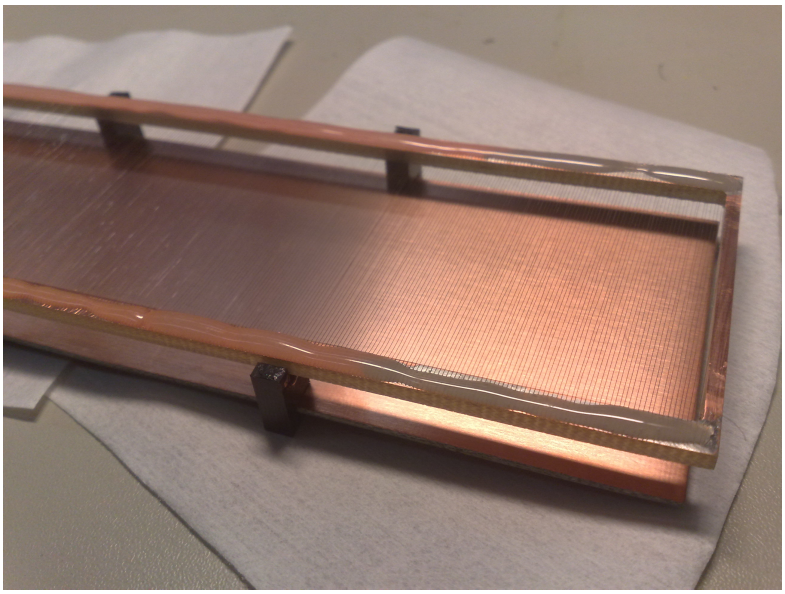

Figure 19: Picture of a Frisch grid after tightening. The wires of 50 µm diameter of this grid are glued using regular epoxy at 0.5 mm intervals on a single sided PCB. The total anode length is 250 mm corresponding to 500 wires. The distance the wires hang unsupported is 40 mm. The insulating black plastic blocks increase the tension of the wires and attach the grid frame to the anode 8 mm below the wire plane.

Alternative process of manufacturing the grid was also attempted. In this process wires are spun on threaded rods and a similar circuit board as previously is glued to the spunned harp. This one-shot process would be slightly easier but in reality yielded looser wires than the method described above.

5.5 Calibration and resolution

5.5.1 Energy calibration

Calibration measurements were initially done with scattered beam from thick sample containing one or more heavy elements, since we detect only a single nuclide, namely the backscattered or forward scattered incident beam. There is no need to

separate different elements and measurements with heavy ions is simplified. These measurements can be used to obtain an energy calibration since the scattered beam has a known maximum energy when indicent beam energy, scattering angle and heaviest sample element are known. This requires multiple measurements with varying incident beam energy, since only one point of calibration is obtained for each measurement.

It is much more convenient to calibrate the gas ionization detector against the energy obtained with time of flight measurement. Now the full spectrum where different masses can be separated can be used to perform calibration. A second order polynomial fit for ^{12}C is plotted in figure 20.

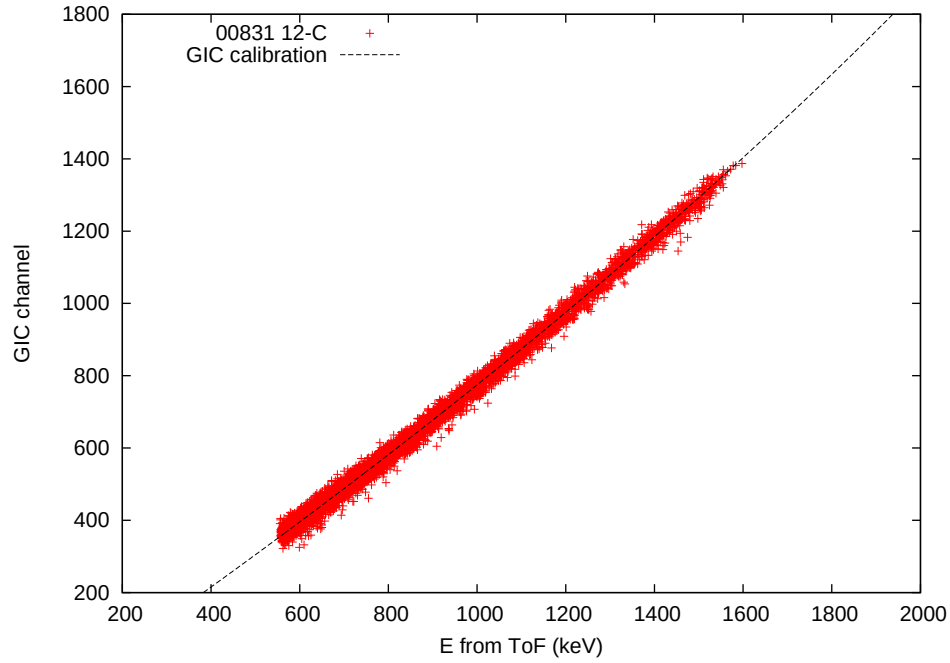

Figure 20: The energy calibration of the GIC for ^{12}C. The fitted polynomial is $E = 152.3\,\mathrm{keV} + 1.172\,\mathrm{keV/ch} \times \mathrm{channel} - 9.981 \cdot 10^{-5}\,\mathrm{keV/ch^2} \times \mathrm{channel}^2$.

5.5.2 Energy resolution

To obtain resolution at some E we can choose events near E and calculate the distribution of $\frac{E_{\mathrm{GIC}}}{E_{\mathrm{TOF}}}$. If time-of-flight measurement is assumed to have better energy resolution in comparison with the GIC measurement, which holds at least for heavy recoils, the deviation from unity is mainly due to the limited resolution of the GIC. The relative error can be then multiplied with E to obtain absolute resolution at E. An example of distribution of values of $\frac{E_{\mathrm{GIC}}}{E_{\mathrm{TOF}}}$ is in figure 21. In figure 22 the resolution of the GIC is plotted for different elements at different energies. Since the noise seems to have very little dependence on energy it is presumed the resolution is limited by electronics noise. This assumption is backed up by the obtained 25 keV resolution for hydrogen, since electronics noise with Ortec 142B preamplifier with W=26.3 eV/pair alone limits the resolution to $2.6\,\mathrm{keV} \times \frac{26.3}{3.63} \approx 19\,\mathrm{keV}$.

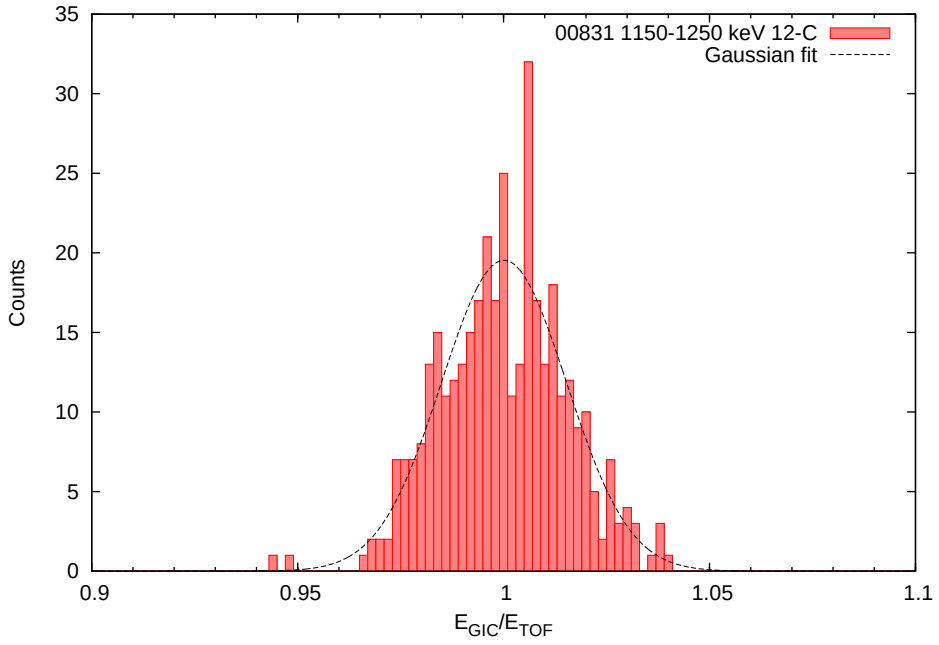

Figure 21: The distribution of calibrated values of $\frac{E_{\mathrm{GIC}}}{E_{\mathrm{TOF}}}$ between 1150 keV and 1250 keV for ^{12}C. The gaussian fit has a mean of 1.0001 and standard deviation of 0.0152, which corresponds to a FWHM resolution of 43 keV at 1200 keV.

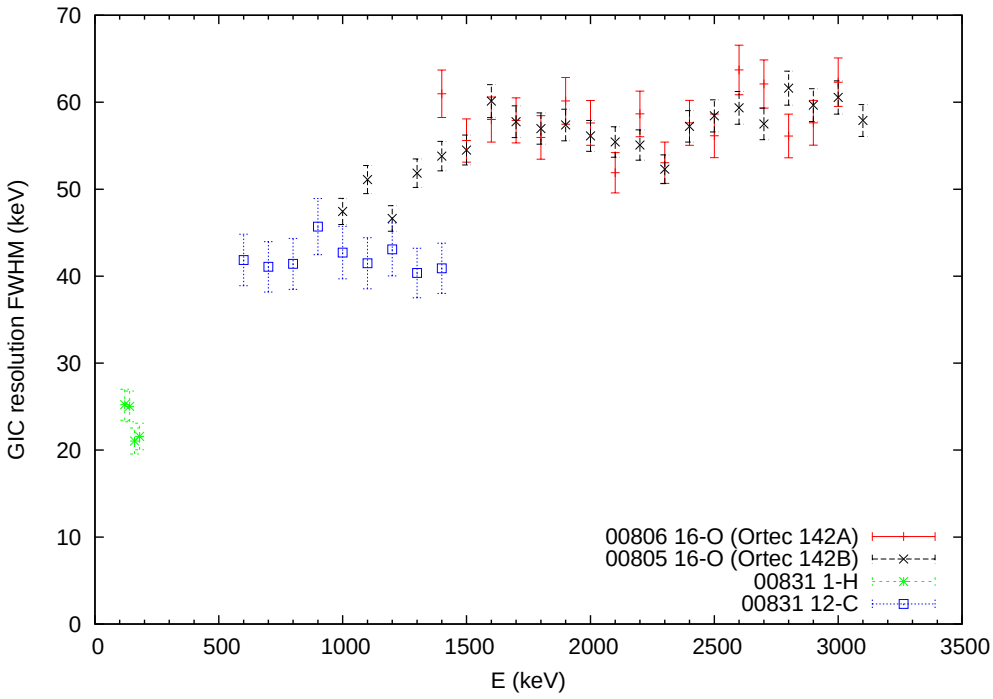

Figure 22: The resolution (FWHM) of the GIC at different energies for ^{1}H, ^{12}C, and ^{16}O. The data for ^{16}O is measured with two different preamplifiers, with similar results. The error bars of resolution values are due to statistical error, other effects such as error in energy calibration have not been taken into account.

The response of each element is different and therefore an individual calibration for each element is necessary if the GIC is used in accurate energy measurements or for resolution calculations. The differences are due to the ionization process, nuclear stopping, energy loss in the entrance window. These effects are collectively known as pulse height defects (PHD), a term more commonly associated with similar processes in silicon detectors. The PHD of silicon detectors has been studied extensively, but there seems to be no accurate theory to compensate for the PHD for all elements and energies. Silicon detectors are often calibrated against known α emitters. The energy of these alpha particles is near 5 MeV, for example of the alpha particles ^{241}Am emits as it decays to ^{237}Np 84.8% have an energy of 5485.56 keV and 13.1% have an energy of 5442.80 keV [40], which can be resolved with silicon detectors if the alpha source is of high quality. The developed GIC is

not particularly suitable for this high energies for alphas. The alpha particles will be barely stopped in the active gas volume by increasing the gas pressure near 70 mbar, a result also supported by SRIM calculations, but even then the detector is not 100% efficient, which results in tailing peaks and loss of resolution. Due to low amount of activity of alpha sources it is also not feasible to do measurements when the source is placed very far away from the detector window. On the other hand placing the source close to the window will cause problems due to geometric spread of the particle tracks.

5.5.3 Mass resolution

Mass can be resolved using equation (18). For this equation to be useful we need to define an energy calibration and a time-of-flight calibration. Time of flight can be simply stated as

$$t = t_0 + t_1 \times \mathrm{TDC}, \tag{20}$$

where TDC is the observed channel number from a time-to-digital converter (TDC), t_0 is an offset from true time of flight due to signal cable length etc and t_1 is the true width of a single channel in the TDC. Direct energy calibration is impossible without information of recoil mass. The energy calibration is therefore a function of the recoil mass number A

$$E = \frac{1}{2}mv^2 = \frac{1}{2}Au\frac{L}{t_0 + t_1 \times \mathrm{TDC}}, \tag{21}$$

where L is the calibrated distance between time-of-flight detectors. This parameter can also be neglected since only two free parameters are used for time-of-flight to energy calibration.

Calibration for the GIC is not so straightforward as the energy response of observed ionization is different for different nuclides. One might attempt to compensate this by introducing mass-dependent terms. For example like in [41]

$$E = (c_0 + c_1 A) + (c_2 + c_3 A)X + (c_4 + c_5 A)X^2, \tag{22}$$

which is a second-order polynomial of X, the ADC channel, with linear mass dependence ($\propto A$) in each term. However entrance window energy loss is strongly

dependant on the charge of the nucleus [31], which means one should also introduce terms depending on the Z of the nucleus. This energy calibration is however adequate for higher energies, when the energy lost in the entrance window is low. Each measurement of (TDC,X) can be converted into mass data solving for A [41]:

$$Au = \frac{c_0 + c_2 + c_4 X^2}{\frac{L^2}{2(t_0 + t_1 \mathrm{TDC})} - c_1 - c_3 X - c_5 X^2}, \tag{23}$$

In order to achieve a good energy calibration function where the mass could be solved an equation similar to 22 was used, with one notable exception. The term $(c_2 + c_3 A)X$ which depends linearly on the channel number and mass number does not correspond well with observations, so a function that does (26) was used instead. The energy calibration equation used was of the form

$$E(Z, A) = a(Z, A) \times X^2 + b(Z, A) \times X + c(Z, A), \tag{24}$$

where

$$a(A) = a_1 A + a_0, \tag{25}$$

$$b(A) = b_1 \left(1 - \exp(-b_2 A)\right) + b_0, \tag{26}$$

$$c(A) = c_1 A + c_0. \tag{27}$$

The calibration parameters $a_0, a_1, b_0, b_1, b_2, c_0$ and c_1 were found by first fitting a polynomial $E = aX^2 + bX + c$ for every mass that can be resolved from a TOF-E spectrum as was done in section 5.5.1. The results of this fit from a measurement of a borosilicate glass sample, where recoils of ^{1}H,^{10}B, ^{11}B, ^{16}O, ^{23}Na ja scattered beam ^{79}Br are assembled to table 1. The table contains the polynomial terms a, b and c for every nuclide, and also the energy range of the fitted data. The fit to ^{1}H was only a first order polynomial ($a = 0$) due to the uncertainty of the second order fit to the narrow energy range. Hydrogen data was neglected when fitting $a(A)$. The fit could be improved by increasing the amount of data points, but since isotopes of heavy elements cannot be separated the use of these for calibration is difficult. Masses between $23 < A < 79$ do fit reasonably well to the calibration, but this calibration should not be extrapolated for $A > 79$.

Table 1: Energy calibration parameters from measurement tof_e_00805

Nuclide	Z	A	a (keV/ch^2)	b (keV/ch)	c (keV)	$E_{\min}$(keV)	$E_{\max}$(keV)
^{1}H	1	1	0	0.68	62	140	290
^{10}B	5	10	-4.5×10^{-5}	1.03	165	800	2300
^{11}B	5	11	-3.8×10^{-5}	1.02	177	800	2500
^{16}O	8	16	-3.4×10^{-5}	1.09	240	1000	3200
^{23}Na	11	23	-3.4×10^{-5}	1.13	220	800	4000
^{79}Br	35	79	-1.4×10^{-5}	1.21	494	2500	7200

Following values were obtained for the calibration parameters:

$$\begin{aligned} a_0 &= -4.06 \times 10^{-5}\,\mathrm{keV/ch^2}, \\ a_1 &= 3.32 \times 10^{-7}\,\mathrm{keV/ch^2}, \\ b_0 &= 0.607\,\mathrm{keV/ch}, \\ b_1 &= 0.583\,\mathrm{keV/ch}, \\ b_2 &= 0.115, \\ c_0 &= 127\,\mathrm{keV}, \\ c_1 &= 4.57\,\mathrm{keV}. \end{aligned}$$

The problem with this energy calibration is that the mass number A is not easily solved from the equations (21) and (24). This limitation can be easily overcome by solving the set of equations in respect to A numerically, for example using Newton's method. Now when every (TDC,X) pair can be solved to give a mass. In figure 23 the resulting mass spectrum is plotted. The data used in the figure is limited to the near-surface region by plotting only the data points where $E > E_{\max}$. This limit is also visible on the figure 24, where the calibrated data is plotted as a two dimensional (E, A) histogram. $E_{\max}$ is the maximum energy $E_{\max} = \frac{4M_1M_2}{(M_1+M_2)^2}\cos^2\phi$ for a given recoil mass. A gaussian fit was done on the ^{39}K peak, which has a FWHM of 0.89 and a mean of 38.1. This gives a mass resolution of $\frac{M}{\Delta M} \approx 42$.

The difference in resolution when the GIC is compared to a Si detector for elements heavier than oxygen is clear from the TOF-E spectum. As an example bulk borosilicate glass was measured using both a mint thin entrance window 450mm^2 silicon detector (Canberra PIPS) and the new gas ionization detector. Experimen-

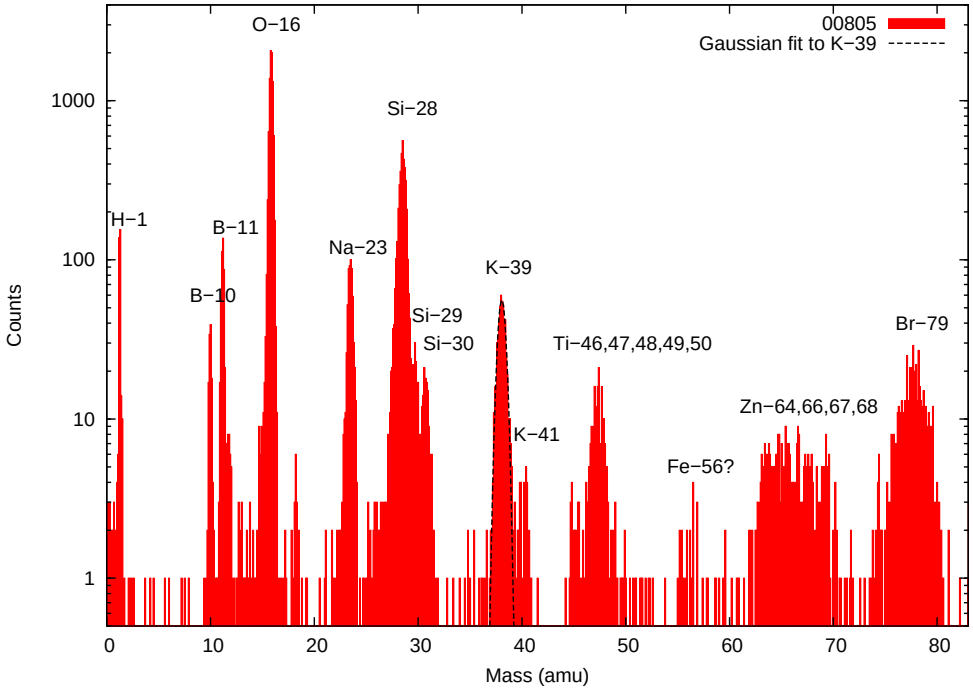

Figure 23: Mass spectrum of a borosilicate glass sample determined from the time-of-flight–energy measurement. A gaussian fit was done on the ^{39}K peak.

tal setup was identical with 10.2 MeV ^{79}Br beam. The larger solid angle of the silicon detector does not affect mass resolution. From figure 25 one can see how the ionization detector outperforms Si detector even for ^{10}B although the resolution of the GIC could still be improved by a factor of two by reducing electronics noise. For heavier recoils and lower energies the difference in resolution is even more pronounced.

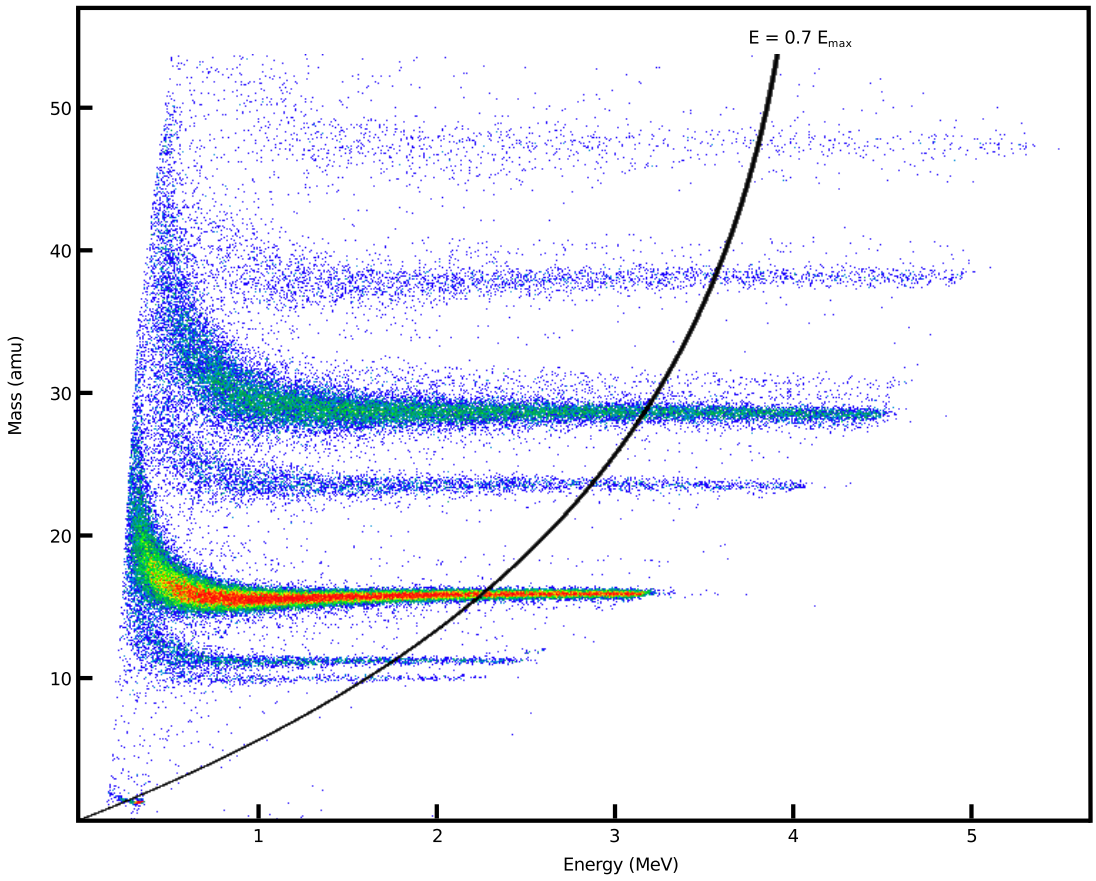

Figure 24: Mass-energy histogram of a borosilicate glass sample that is obtained after data has been calibrated. The line corresponds to $E = 0.7 \times E_{\max}$ to give a visual clue of where the important near-surface region ($E \approx E_{\max}$) is.

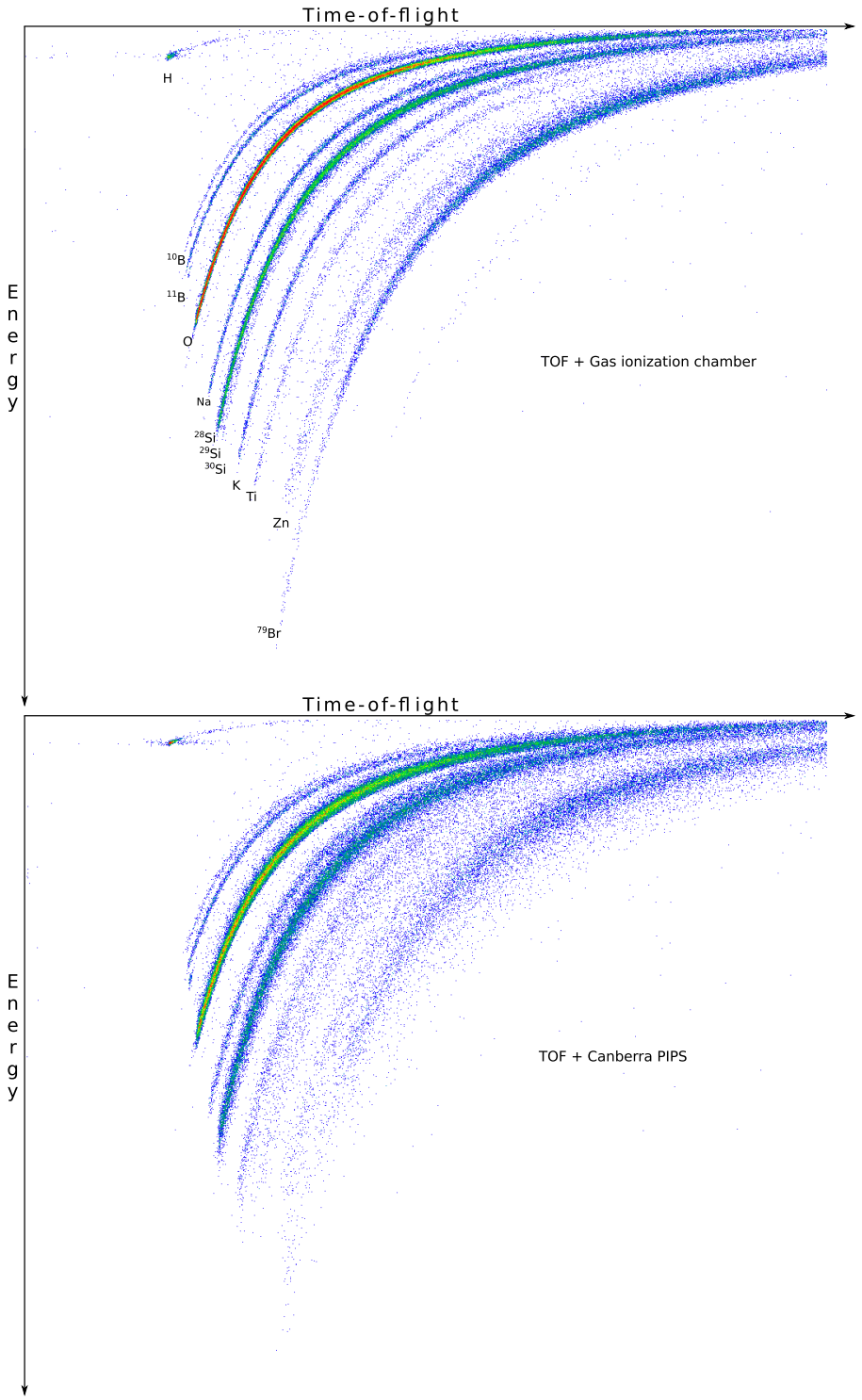

Figure 25: ERD measurement of a borosilicate glass sample with 10.2 MeV ^{79}Br incident beam. The spectrum on the top is measured with the GIC and the one on the bottom with a pristine Canberra PIPS silicon detector. Otherwise the same telescope and similar statistics were used. The mass resolution with the GIC is clearly better.

5.5.4 Position resolution

Position sensitivity is demonstrated in figure 26. This measurement was performed with 5.5 MeV alpha particles emitted by ^{241}Am source and a collimator with three 1 mm wide slits 3 mm apart from each other. The cathode signal was also acquired in the ERD measurements done with the detector. The 5 mm wide window was not large enough to clearly demonstrate position sensitivity with the obtained energy or cathode resolution. The cathode signals were successfully acquired in coincidence with the anode signal and a linear dependence between them was observed. Had the position resolution been a major focus a collimator should have been placed before the window, but this was prevented due to lack of measurement time and larger windows.

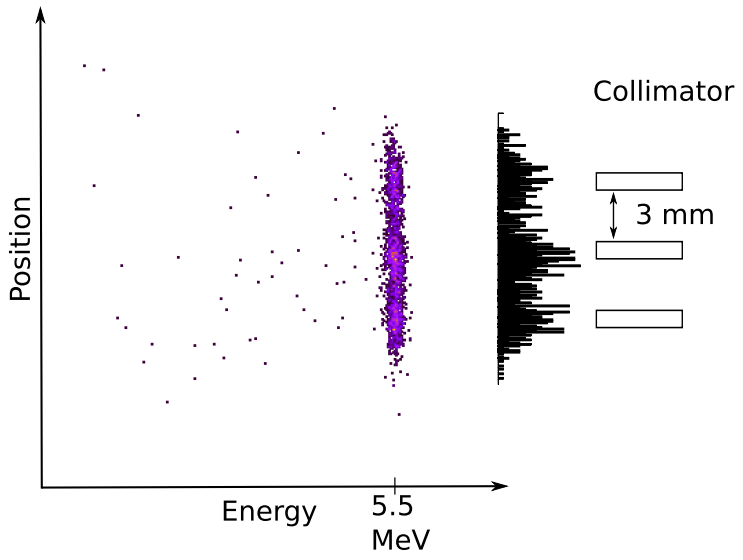

Figure 26: Position sensitivity demonstrated with a collimator near entrance window for 5.5 MeV alphas from Am-241 source. Energy resolution of the detector was further improved after these measurements. The position axis is simply cathode ADC signal divided by the anode ADC signal (energy) without any correction. Brighter colors stand for higher intensity in the 2D histogram. The projected 1D position histogram is also plotted.

5.6 Data aqcuisition and coincidence processing

In TOF-E measurements data was acquired by means of a National Instruments FPGA data acquisition system which reads time-of-flight from a FAST ComTec 7072T TDC (ADC0) and energy signal from another channel of the same device operating as an ADC (ADC1). The TDC/ADC has a 500 ns fixed conversion time 13-bit ADC. Additionally cathode signal was acquired from another ADC (ADC2). There is no triggering between ADC0, ADC1 or ADC2 events, but the events are timestamped with 25 ns precision by the FPGA, which corresponds to one clock tick at 40 MHz.

A piece of software was written to do the offline coincidence processing. The program works by attempting to find the closest ADC1 (E) event to every ADC0 (TOF) event inside a given time window. The program can find false coincidences but does not lose any real coincidences, since there cannot be two energy counts inside the same timing window due to the TDC conversion time of 500 ns and ADC dead time between 1 and 3 µs if the spectroscopy amplifier has pile-up rejection. Coincidences are processed so that all ADC0 events within the timing window for a given ADC1 event are found.

In figure 27 a histogram of timestamp differences is plotted with a gaussian fit. It can be seen that most of the 114000 counts fall inside the bell curve which has an area corresponding to 105000 counts. Most of the counts outside the gaussian fit come from the fact that the timing accuracy of the energy detector is energy dependant. The timing is done between the TDC and ADC events. Spectroscopy amplifier output pulse does have predictable rise time from zero level to maximum assuming there is no pile-up and the ADC conversion starts some time after the maximum. Low frequency noise in the spectroscopy amplifier output will cause timing jitter by delaying or advancing the start of conversion. This error is larger for small pulse heights due to the gaussian shape and therefore also proportional to the shaping time. In figure 28 an intensity map of ADC1 values versus timestamp difference to ADC0 are plotted.

By choosing a tight window we can eliminate some of the false coincidences but choosing too tight a window can result in unwanted statistical bias. In ERD measurements the low energy end is important due to small signals from hydrogen.

Coincidence window could also be set so that it is wider for the TOF range where hydrogen signal is observed. Improvement in the background noise elimination requires good timing properties and short pulses from the detector. In this situation thin silicon detectors – particularly those which have improved timing properties – outperform gas ionization detector. The timing accuracy can also be improved by employing digital pulse processing instead of the conventional analog electronics chain.

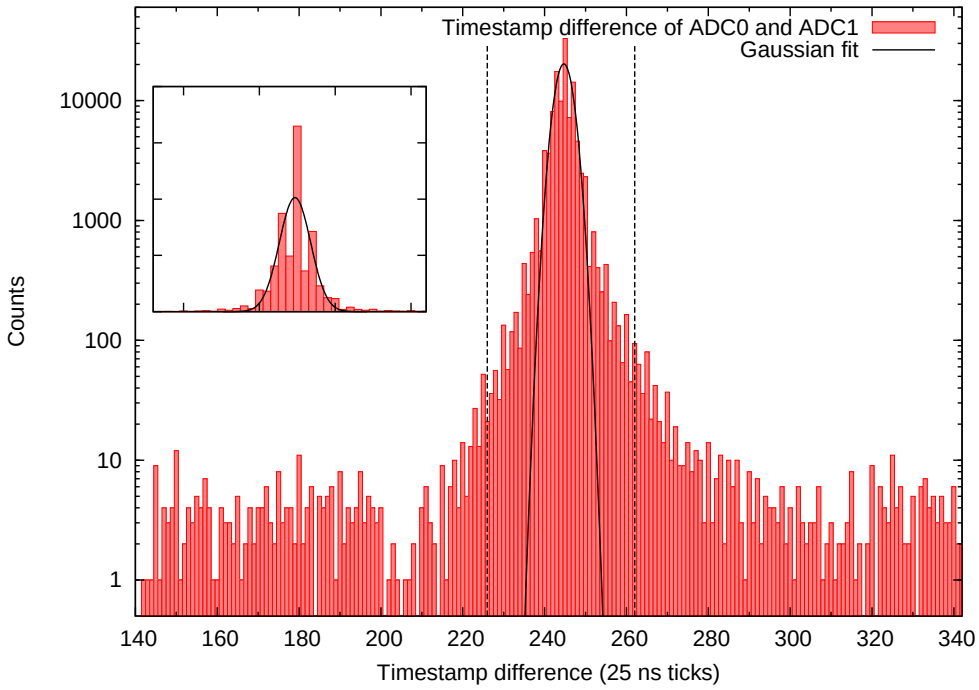

Figure 27: Timestamp difference between ADC0 (time-of-flight) and ADC1 (energy). The timing window used for this measurement is marked with vertical lines at ticks 226 and 262. There is a nearly constant background outside the peak. A gaussian fit is attempted on the peak, the mean is 244.7 ticks, standard deviation 2.1 ticks and area 105000 counts. There are a total of 114492 counts plotted between 140 and 340 ticks. The inset shows the same peak from ticks 226 to 262 on a linear vertical scale.

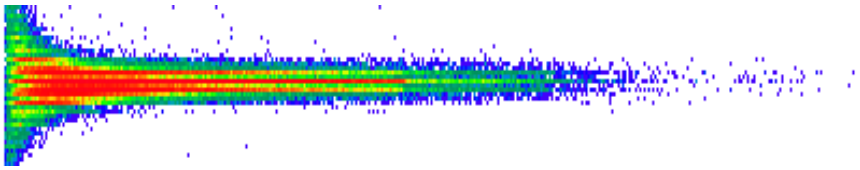

Figure 28: 2D Timestamp difference histogram between ADC0 (time-of-flight) and ADC1 (energy) on vertical axis as a function of ADC1 on the horizontal axis. Timing window is set so that events with a time difference between 226 and 262 ticks are accepted. One tick is 25 ns making the window 900 ns wide. There are some events visible that are clearly outside the peak, but the majority of wrong coincidences are cut off. Events appear on the ADC output at different times due to long drift time as seen in figure 17 and the shaping time of the spectroscopy amplifier with the latter being dependant on the former.

6 Conclusions

Gas ionization chambers are definitely the future of lower energy HI-TOF-ERD currently carried out with planar silicon detectors as energy detectors. Silicon detectors can outperform GICs in hydrogen and helium resolution, which in most cases is not critical anyway as hydrogen and helium are the easiest elements to separate. Hydrogen detection for GICs is not a problem for low energy ERD since GICs with thin silicon nitride windows are able to detect even low energy (≈ 200 keV) hydrogen efficiently.

For most real world setups gas ionization chamber will improve resolution immensely, and planar silicon detector can be simply replaced by a GIC without further modifications to the measurement setup. If low energy stopping and cross-section information is available reliably TOF-ERD with good timing resolution and a high energy resolution GIC can be used to achieve high resolution quantitative near-surface depth profiling of all elements.

The design of a good GIC requires careful simulations and finding the right compromise for each individual measurement setup. Still the mechanical construction is simple and sets no special requirements on materials or expertise apart from the silicon nitride entrance window. As silicon nitride windows have become more easily available there should be renewed interest in GICs as a universal tool for ion beam based materials physics.

7 References

[1] J. L'Ecuyer, C. Brassard, C. Cardinal, J. Chabbal, L. Deschênes, J. P. Labrie, B. Terreault, J. G. Martel, and R. St.-Jacques. An accurate and sensitive method for the determination of the depth distribution of light elements in heavy materials. *Journal of Applied Physics*, 47(1):381–382, 1976.

[2] W. Bohne, J. Röhrich, and G. Röschert. The new time-of-flight ERDA setup at the HMI-Berlin. *Nuclear Instruments and Methods in Physics Research Section B: Beam Interactions with Materials and Atoms*, 139(1-4):219 – 224, 1998.

[3] W. Assmann, P. Hartung, H. Huber, P. Staat, H. Steffens, and Ch. Steinhausen. Setup for materials analysis with heavy ion beams at the Munich MP tandem. *Nuclear Instruments and Methods in Physics Research Section B: Beam Interactions with Materials and Atoms*, 85(1-4):726 – 731, 1994.

[4] H. Timmers, R. G. Elliman, G. R. Palmer, T. R. Ophel, and D. J. O'Connor. The development of a facility for heavy-ion elastic recoil detection analysis at the Australian National University. *Nuclear Instruments and Methods in Physics Research Section B: Beam Interactions with Materials and Atoms*, 136-138:611 – 615, 1998. Ion Beam Analysis.

[5] R. Groleau, S.C. Gujrathi, and J.P. Martin. Time-of-flight system for profiling recoiled light elements. *Nuclear Instruments and Methods in Physics Research*, 218(1-3):11 – 15, 1983.

[6] C.R. Gossett. Use of a magnetic spectrometer to profile light elements by elastic recoil detection. *Nuclear Instruments and Methods in Physics Research Section B: Beam Interactions with Materials and Atoms*, 15(1-6):481 – 485, 1986.

[7] G. Dollinger, M. Boulouednine, T. Faestermann, and P. Maier-Komor. Depth microscopy for thin film analysis. *Nuclear Instruments and Methods in Physics Research Section A: Accelerators, Spectrometers, Detectors and Associated Equipment*, 334(1):187 – 190, 1993.

[8] W. Assmann. Ionization chambers for materials analysis with heavy ion beams. *Nuclear Instruments and Methods in Physics Research Section B: Beam Interactions with Materials and Atoms*, 64(1-4):267 – 271, 1992.

[9] G. Pausch, W. Bohne, and D. Hilscher. Particle identification in solid-state detectors by means of pulse-shape analysis – results of computer simulations. *Nuclear Instruments and Methods in Physics Research Section A: Accelerators, Spectrometers, Detectors and Associated Equipment*, 337(2-3):573 – 587, 1994.

[10] S. Giangrandi, T. Sajavaara, B. Brijs, K. Arstila, A. Vantomme, and W. Vandervorst. Low-energy heavy-ion TOF-ERDA setup for quantitative depth profiling of thin films. *Nuclear Instruments and Methods in Physics Research Section B: Beam Interactions with Materials and Atoms*, 266(24):5144 – 5150, 2008.

[11] C. Kottler, M. Döbeli, F. Glaus, and M. Suter. A spectrometer for low energy heavy ion ERDA. *Nuclear Instruments and Methods in Physics Research Section B: Beam Interactions with Materials and Atoms*, 248(1):155 – 162, 2006.

[12] M. Laitinen, T. Sajavaara, M. Rossi, J. Julin, R.L. Puurunen, T. Suni, T. Ishida, H. Fujita, K. Arstila, B. Brijs, and H.J. Whitlow. Depth profiling of $Al_2O_3+TiO_2$ nanolaminates by means of a time-of-flight energy spectrometer. *Nuclear Instruments and Methods in Physics Research Section B: Beam Interactions with Materials and Atoms*, In Press, Accepted Manuscript:–, 2011.

[13] J. R. Tesmer and M. Nastasi. *The Handbook of Modern Ion Beam Materials Analysis*. Materials Research Society, 1995.

[14] H. Bethe. Bremsformel für elektronen relativistischer geschwindigkeit. *Zeitschrift für Physik*, 76:293–299, 1932.

[15] F. Bloch. Bremsvermögen von atomen mit mehreren elektronen. *Zeitschrift für Physik*, 81:363–376, 1933.

[16] J. Ziegler. The Stopping and Range of Ions in Matter (SRIM). `http://www.srim.org/`.

[17] J. S. Lilley. *Nuclear Physics: Principles and Applications*. John Wiley & Sons, New York, 2001.

[18] W. K. Chu. Calculation of energy straggling for protons and helium ions. *Phys. Rev. A*, 13(6):2057–2060, Jun 1976.

[19] Q. Yang, D.J. O'Connor, and Zhonglie Wang. Empirical formulae for energy loss straggling of ions in matter. *Nuclear Instruments and Methods in Physics Research Section B: Beam Interactions with Materials and Atoms*, 61(2):149 – 155, 1991.

[20] G. F. Knoll. *Radiation Detection and Measurement*. John Wiley & Sons, New York, 3rd edition, 2000.

[21] K. Kleinknecht. *Detectors for Particle Radiation*. Cambridge University Press, second edition, 1998.

[22] U. Fano. Ionization yield of radiations. II. The fluctuations of the number of ions. *Phys. Rev.*, 72(1):26–29, 1947.

[23] Martin Suter, Max Döbeli, Michal Grajcar, Arnold Müller, Martin Stocker, Guoyan Sun, Hans-Arno Synal, and Lukas Wacker. Advances in particle identification in AMS at low energies. *Nuclear Instruments and Methods in Physics Research Section B: Beam Interactions with Materials and Atoms*, 259(1):165 – 172, 2007. Accelerator Mass Spectrometry - Proceedings of the Tenth International Conference on Accelerator Mass Spectrometry.

[24] B. Rossi and H. Staub. *Ionization Chambers and Counters*. McGraw-Hill Book Company, Inc., first edition, 1949.

[25] W. Shockley. Currents to conductors induced by a moving point charge. *Journal of Applied Physics*, 9, 1938.

[26] O. Frisch. Isotope analysis of uranium samples by means of their α-ray groups. British Atomic Energy Project Report BR-49, 1944. Unpublished.

[27] P. S. Barbeau, J. I. Collar, J. D. Geissinger, J. Miyamoto, I. Shipsey, and R. Yang. A first mass production of gas electron multipliers. *Nuclear Instruments and Methods in Physics Research Section A: Accelerators, Spectrometers, Detectors and Associated Equipment*, 515(3):439 – 445, 2003.

[28] M. Mallepell, M. Döbeli, and M. Suter. Annular gas ionization detector for low energy heavy ion backscattering spectrometry. *Nuclear Instruments and*

Methods in Physics Research Section B: Beam Interactions with Materials and Atoms, 267(7):1193 – 1198, 2009.

[29] A.M. Müller, A. Cassimi, M. Döbeli, M. Mallepell, I. Monnet, M.J. Simon, M. Suter, and H.-A. Synal. A new mini gas ionization chamber for IBA applications. *Nuclear Instruments and Methods in Physics Research Section B: Beam Interactions with Materials and Atoms*, In Press, Accepted Manuscript:–, 2011.

[30] M. Döbeli, C. Kottler, M. Stocker, S. Weinmann, H. A. Synal, M. Grajcar, and M. Suter. Gas ionization chambers with silicon nitride windows for the detection and identification of low energy ions. *Nuclear Instruments and Methods in Physics Research Section B: Beam Interactions with Materials and Atoms*, 219-220:415 – 419, 2004. Proceedings of the Sixteenth International Conference on Ion Beam Analysis.

[31] G. Sun, M. Döbeli, A.M. Müller, M. Stocker, M. Suter, and L. Wacker. Energy loss and straggling of heavy ions in silicon nitride in the low MeV energy range. *Nuclear Instruments and Methods in Physics Research Section B: Beam Interactions with Materials and Atoms*, 256(2):586 – 590, 2007.

[32] Silson Ltd. `http://www.silson.com/`.

[33] V. A. Khriachkov, A. A. Goverdovski, V. V. Ketlerov, V. F. Mitrofanov, and N. N. Semenova. Direct experimental determination of frisch grid inefficiency in ionization chamber. *Nuclear Instruments and Methods in Physics Research Section A: Accelerators, Spectrometers, Detectors and Associated Equipment*, 394(1-2):261 – 264, 1997.

[34] O. Bunemann, T.E. Cranshaw, and J. A. Harvey. Design of Grid Ionization Chambers. *Canadian Journal of Research*, 27, 1949.

[35] SIMION 8. `http://www.simion.com/`.

[36] D. Green. *The Physics of Particle Detectors*. Cambridge University Press, 2000.

[37] O. Forstner, L. Michlmayr, M. Auer, R. Golser, W. Kutschera, A. Priller, P. Steier, and A. Wallner. Applications of a compact ionization chamber in AMS at energies below 1 MeV/amu. *Nuclear Instruments and Methods in*

Physics Research Section B: Beam Interactions with Materials and Atoms, 266(10):2213 – 2216, 2008. Accelerators in Applied Research and Technology - Proceedings of the 9th European Conference on Accelerators in Applied Research and Technology, 9th European Conference on Accelerators in Applied Research and Technology.

[38] H. Timmers, T. R. Ophel, and R. G. Elliman. Simplifying position-sensitive gas-ionization detectors for heavy ion elastic recoil detection. *Nuclear Instruments and Methods in Physics Research Section B: Beam Interactions with Materials and Atoms*, 161-163:19 – 28, 2000.

[39] A. Göpfert, F. J. Hambsch, and H. Bax. A twin ionization chamber setup as detector for light charged particles with energies around 1 MeV applied to the $^{10}\mathrm{B}(\mathrm{n},\alpha)^{7}\mathrm{Li}$ reaction. *Nuclear Instruments and Methods in Physics Research Section A: Accelerators, Spectrometers, Detectors and Associated Equipment*, 441(3):438 – 451, 2000.

[40] M.S. Basunia. Nuclear Data Sheets for A = 237. *Nuclear Data Sheets*, 107(8):2323 – 2422, 2006.

[41] M. E. Bouanani, M. Hult, L. Persson, E. Swietlicki, M. Andersson, M. Östling, N. Lundberg, C. Zaring, D. D. Cohen, N. Dytlewski, P. N. Johnston, S. R. Walker, I. F. Bubb, and H. J. Whitlow. Multivariate analysis method for energy calibration and improved mass assignment in recoil spectrometry. *Nuclear Instruments and Methods in Physics Research Section B: Beam Interactions with Materials and Atoms*, 94(4):530 – 536, 1994.